

# We are IntechOpen, the world's leading publisher of Open Access books Built by scientists, for scientists

6,900

Open access books available

186,000

International authors and editors

200M

Downloads

Our authors are among the

154

Countries delivered to

TOP 1%

most cited scientists

12.2%

Contributors from top 500 universities



WEB OF SCIENCE™

Selection of our books indexed in the Book Citation Index  
in Web of Science™ Core Collection (BKCI)

Interested in publishing with us?  
Contact [book.department@intechopen.com](mailto:book.department@intechopen.com)

Numbers displayed above are based on latest data collected.  
For more information visit [www.intechopen.com](http://www.intechopen.com)



# Nanostructuring Bi<sub>2</sub>Te<sub>3</sub>-Based Thermoelectric Thin-Films Grown Using Pulsed Laser Deposition

*Le Thi Cam Tuyen, Phuoc Huu Le and Sheng-Rui Jian*

## Abstract

This book chapter reports recent advances in nanostructured Bi<sub>2</sub>Te<sub>3</sub>-based thermoelectric (TE) thin-films fabricated by pulsed laser deposition (PLD). By controlling the processing conditions in PLD growths, various fascinating Bi<sub>2</sub>Te<sub>3</sub>-based nanostructured films with promising or enhanced TE properties have been successfully fabricated, including super-assembling of Bi<sub>2</sub>Te<sub>3</sub> hierarchical nanostructures, self-assembled Bi<sub>2</sub>Te<sub>3</sub> films with well-aligned 0D to 3D nanoblocks, polycrystalline-nanostructured Bi<sub>2</sub>Se<sub>3</sub> and Bi<sub>2</sub>Te<sub>3</sub> thin-films, etc. In addition, a PLD-growth mechanism for fabricating the super-assembling Bi<sub>2</sub>Te<sub>3</sub> thin-films is presented. This book chapter provides fundamental understanding the relationship amongst processing condition, structure-morphology, and TE property of PLD-growth Bi<sub>2</sub>Te<sub>3</sub>-based thin-films. It also presents an overview of TE materials and applications with the challenges and perspectives.

**Keywords:** Bi<sub>2</sub>Te<sub>3</sub>, thermoelectrics, self-assembly nanostructures, thermoelectric power factor, pulsed laser deposition

## 1. Introduction

Thermoelectric materials are solid-state energy converters whose combination of thermal, electrical, and semiconducting properties allows them to be used to convert waste heat into electricity or electrical power directly into cooling and heating [1].

### 1.1 Thermoelectric effects

When an electric current flows through a pair of p-type and n-type semiconductors connected in series (**Figure 1(a)**), the holes in the p-type material and the electrons in the n-type material carry heat away from the top metal–semiconductor junctions, which leads to a cooling at the junctions called the Peltier effect. When current flows within the module, one side is cooled and the other heated. If the current is reversed, the hot and cold sides reverse also. For each material, the cooling effect is gauged by the Peltier coefficient  $\Pi$  that relates the heat carried by the charges to the electrical current through [1, 2, 4]:  $Q = \Pi \times I$ .

In **Figure 1(b)**, when the two ends of the materials maintain a temperature difference, the higher thermal energy holes and electrons will diffuse from the hot

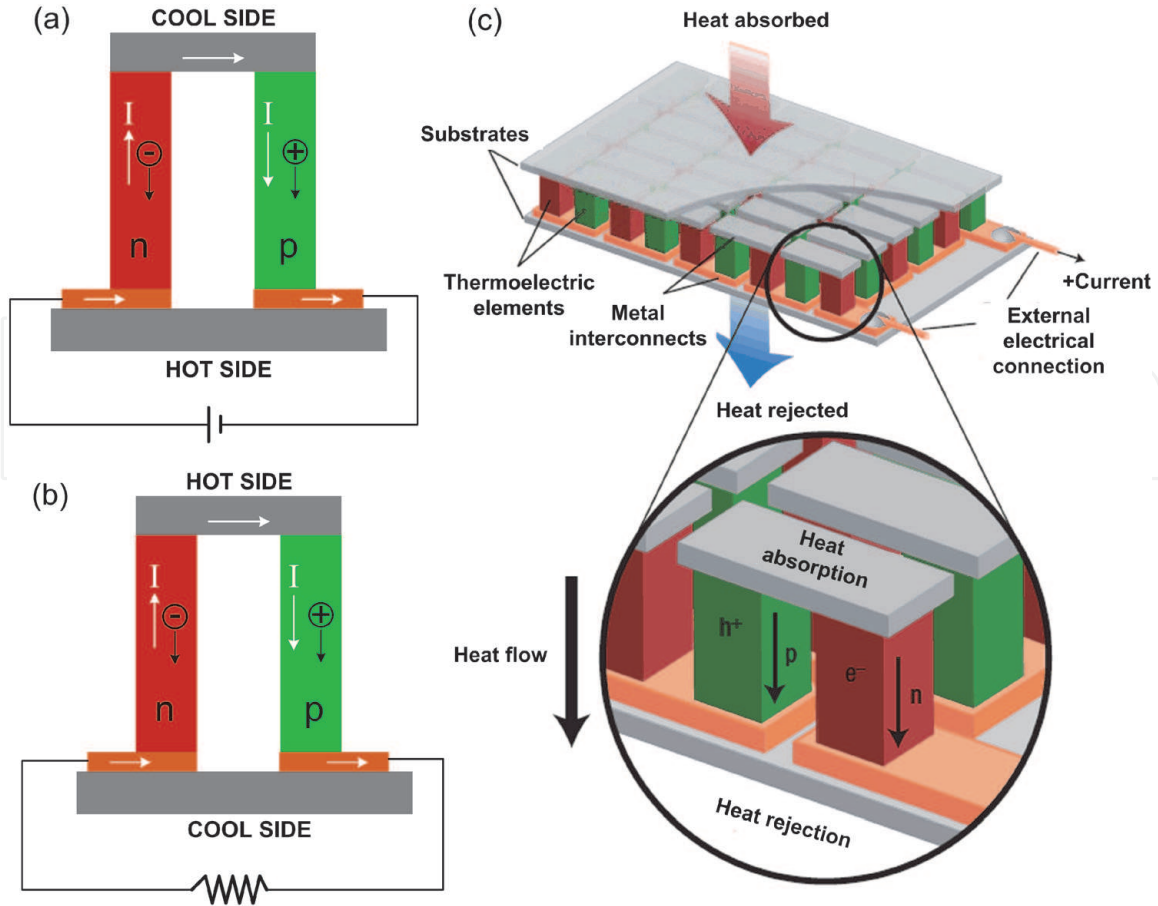


**Figure 1.**

Illustration of TE devices: (a) cooler (Peltier effect), (b) power generator (Seebeck effect). Redrawn after Ref. [2]. (c) Thermoelectric module showing the direction of charge flow on both cooling and power generation [3].

side to the cold side, and consequently a potential difference is created. This is Seebeck effect and it is the principle for thermocouples. The power generation is measured by the Seebeck coefficient  $\alpha$ , which relates the voltage generated to the temperature difference through  $\Delta V = -\alpha\Delta T$ . The Peltier and the Seebeck coefficients are related through the Kelvin relation [1, 2]:  $\Pi = \alpha T$ .

Thermoelectric devices contain many thermoelectric couples (**Figure 1c**, bottom), which consist of p-type (containing free holes) and n-type (containing free electrons) thermoelectric elements connected electrically in series and thermally in parallel (**Figure 1c**, top). A thermoelectric generator uses heat flow across a temperature gradient to power an electric load through the external circuit.

## 1.2 The thermoelectric figure of merit (ZT)

The performance of the thermoelectric materials is often denoted as figure of merit  $Z$  whose unit is  $K^{-1}$ , or  $ZT$  the dimensionless unit [5, 6].

$$ZT = \frac{\alpha^2 \sigma}{\kappa} T = \frac{\alpha^2 \sigma}{\kappa_E + \kappa_L} T \quad (1)$$

where  $\alpha$ ,  $\sigma$ ,  $T$ , and  $\kappa$  are the Seebeck coefficient, electrical conductivity, absolute temperature, and thermal conductivity, respectively. The total thermal conductivity can be split into electronic contribution ( $\kappa_E$ ) and lattice contribution ( $\kappa_L$ ). The thermoelectric power factor (PF) is calculated by the quantity of  $\alpha^2 \sigma$ . The efficiency of a thermoelectric material is determined by its  $ZT$ . Meanwhile, the maximum efficiency ( $\eta$ ) of a power generation is expressed by [3, 7]:

$$\eta = \frac{T_h - T_c}{T_h} \cdot \frac{\sqrt{1 + Z\bar{T}} - 1}{\sqrt{1 + Z\bar{T}} + \frac{T_c}{T_h}} \quad (2)$$

and the coefficient of performance presents for the efficiency of air-conditioning and refrigeration [7]:

$$\text{COP} = \frac{T_c}{T_h - T_c} \cdot \frac{\sqrt{1 + Z\bar{T}} - \frac{T_h}{T_c}}{\sqrt{1 + Z\bar{T}} + 1} \quad (3)$$

where  $T_h$  and  $T_c$  are the hot-end and cold-end temperature of the thermoelectric materials, respectively, and  $\bar{T}$  is the average temperature of  $T_h$  and  $T_c$ . For practical applications, it is important to use high ZT thermoelectric materials.

The best materials so far are alloys of  $\text{Bi}_2\text{Te}_3$  with  $\text{Sb}_2\text{Te}_3$  and  $\text{Bi}_2\text{Te}_3$  with  $\text{Bi}_2\text{Se}_3$ . ZT is of the order of 1 at room temperature. This value gives a COP of about 1 (Figure 2a), which is still far lower than the COP = 2–4 of household refrigerators and air conditioners. Similar situation is true for power generation (Figure 2b) [2, 8]. Thermoelectric cooling and power generation generally still not competitive with the other energy conversion methods.

### 1.3 Challenges in enhancing ZT

A concept of “phonon-glass electron-crystal” (or PGEC in short) was proposed for designing efficient thermoelectric materials. This is a controversial concept from the aspect of materials science that the materials should have a high electrical conductivity as in a crystal and a low lattice thermal conductivity as in a glass [9]. However, the TE parameters are strongly interdependent, which makes the enhancement efforts of ZT very challenging. A normal approach for the enhanced properties of TE materials is to increase the power factor  $\alpha^2\sigma$  by optimizing the carrier concentration  $n$ , and/or to reduce the lattice thermal conductivity  $\kappa_L$  by introducing the scattering centers. These parameters are the function of carrier effective mass  $m^*$  and carrier mobility  $\mu$ , scattering factor  $r$ , and their interconnectivity limit ZT to approximately 1 in large bulk materials [10].

The kinetic definition of  $\alpha$  is the energy difference between the average energy of mobile carriers and the Fermi energy [11]. When carrier concentration ( $n$ ) is increased, both the Fermi energy and the average energy increase, but the Fermi energy increases more rapidly than the average energy as  $n$  is increased. Consequently,  $\alpha$  decreases and thus  $\alpha^2n$  is dragged down rapidly. Therefore, the carrier

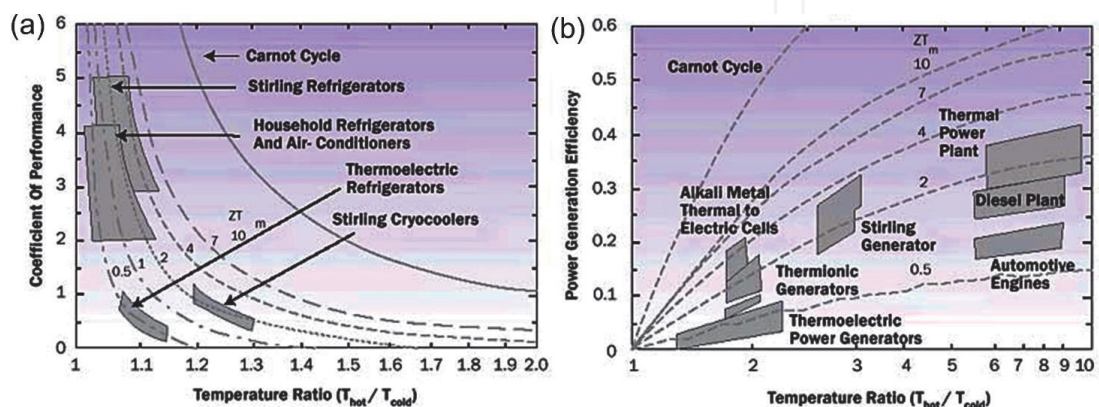


**Figure 2.** Comparison of thermoelectric technology with other energy conversion methods for (a) cooling and (b) power generation [2, 8].

concentration ( $n$ ) increases electrical conductivity ( $\sigma$ ) but reduces the Seebeck coefficient ( $\alpha$ ) for most of the homogeneous materials. For this reason, in metals and degenerate semiconductors with energy-independent scattering approximation, the Seebeck coefficient can be expressed as [3, 12]:

$$\alpha = \frac{8\pi^2 k_B^2}{3eh^2} m^* T \left( \frac{\pi}{3n} \right)^{2/3} \quad (4)$$

Where, the parameter  $m^*$  is density of states effective mass, and an increase of  $m^*$  can raise the Seebeck coefficient according to the Eq. (4). However, most high  $m^*$  materials have generally low  $\mu$  which limits the  $\alpha$  by a weighted mobility with a factor proportional to  $(m^*)^{3/2}\mu$ . Moreover, there is no such thing as an optimal effective mass. There are high mobility low effective mass semiconductors (SiGe, GaAs) as well as low mobility high effective mass polaron conductors (oxides, chalcogenides) [3].

Noticeably, the defects scatter not only the phonons but also the electrons. When a thermoelectric material is designed for reducing lattice thermal conductivity, its carrier mobility is usually suppressed. Hence, the ratio of  $\mu/\kappa_L$  determines the improvement of ZT [5, 10]. The ratio is observed to increase experimentally through a more reduction in  $\kappa_L$  rather than that in  $\mu$ , but some fundamental issues in this mechanism are not understood well [10].

The electrical resistivity ( $\rho$ ) and electrical conductivity ( $\sigma$ ) are related to  $n$  through the carrier mobility  $\mu$ :

$$1/\rho = \sigma = ne\mu \quad (5)$$

The electronic contribution to the thermal conductivity is proportional to the electrical conductivity ( $\sigma$ ) of the materials according to Wiedemann–Franz Law [3], and the relationship is expressed as follows:

$$\kappa_e = L\sigma T = ne\mu LT \quad (6)$$

where ‘e’ is electron charge, and  $L$  is Lorenz factor  $2.48 \times 10^{-8} \text{ J}^2/\text{K}^2\text{C}^2$  for free electrons and this can vary particularly with carrier concentration [3, 13].

**Figure 3** shows the compromise of  $\sigma$ ,  $\kappa$  and  $\alpha$  in thermoelectric materials that must be optimized to maximize the figure of merit ZT. Indeed, the lower carrier concentration will result in the lower  $\sigma$  and a decreasing ZT. Typically, the PF and ZT peaks occur at carrier concentrations of  $10^{19}$ – $10^{21} \text{ cm}^{-3}$  (depending on the material system), which falls in between common metals and heavily doped semiconductors [3]. High mobility carriers are most important for high value of electrical conductivity. Again from the Eq. (4), an increase of the carrier effective mass lead to increase the  $\alpha$  but reduce the  $\mu$  and hence the  $\sigma$  according to the Eq. (5). In case of the narrow semiconductor, the thermal excitation of carrier from valence band to conduction band creates holes and electrons. However, the concentration of the major carrier does not vary much. When two types of carriers are present, or bipolar effects takes place, and this is notorious to achieve effective thermoelectrics [4]. For example, the Seebeck coefficient for different carrier types is given by a weighted average of their electrical conductivity values ( $\sigma_e$  and  $\sigma_p$ ) [13].

$$\alpha \approx \frac{\alpha_e \sigma_e + \alpha_p \sigma_p}{(\sigma_e + \sigma_p)} \quad (7)$$

In short, any attempt to increase  $\sigma$ , will increase  $\kappa_e$  which contributes to thermal conductivity ( $\kappa$ ). In order to counter the increment of  $\kappa_e$ , various approaches are

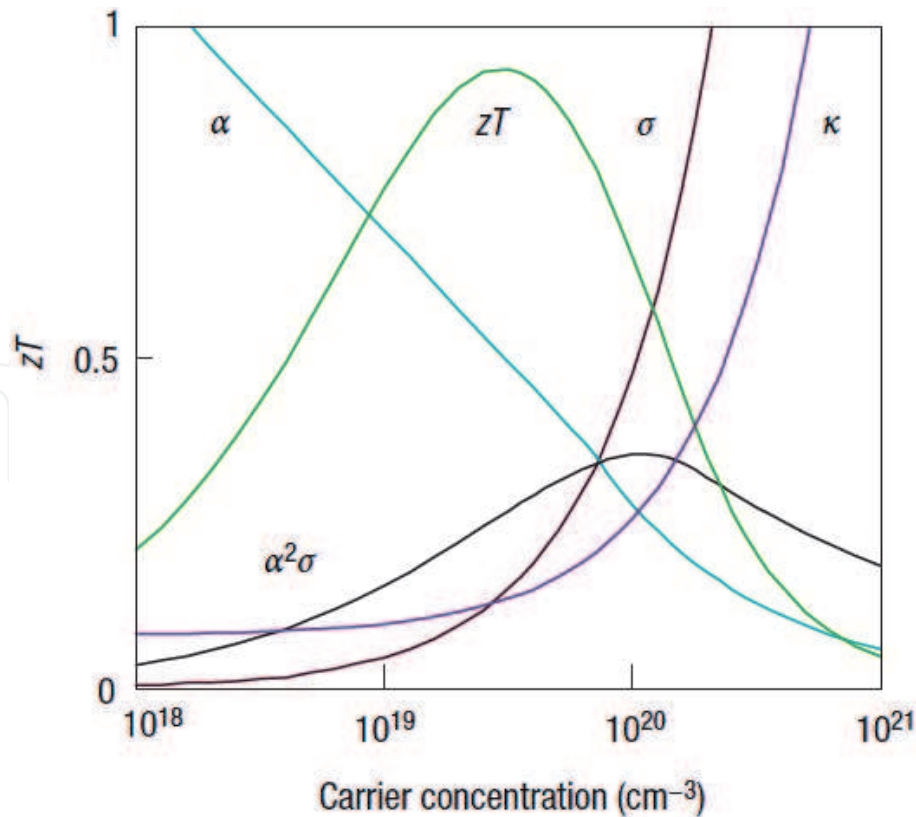


**Figure 3.**

Maximizing the efficiency ( $ZT$ ) of a thermoelectric involves a compromise of thermal conductivity ( $\kappa$ ; plotted on the y-axis from 0 to a top value of  $10 \text{ Wm}^{-1} \text{ K}^{-1}$ ) and Seebeck coefficient ( $\alpha$ ;  $0-500 \mu\text{VK}^{-1}$ ) with electrical conductivity ( $\sigma$ ;  $0-5000 \Omega^{-1} \text{ cm}^{-1}$ ) [3].

reported to reduce  $\kappa_L$ . However, decreasing  $\kappa_L$  with phonon scattering by adding defects results in decrease in  $n$  and  $\sigma$ . These are the major conflicts in the properties of bulk thermoelectric materials which have been addressed in the researches for more than a half century [10].

#### 1.4 Nanostructuring thermoelectric materials

In classical physics, the coefficients  $\alpha$ ,  $\kappa_e$  and  $\sigma$  are interrelated in such a way that it is impossible to increase one without affecting the others. Therefore, a compromise has to be achieved to find the maximum  $ZT$  value. Three different strategies have appeared to improve the  $ZT$  [14]:

- An approach for increasing  $\alpha$  while keeping the values of  $\sigma$  and  $\kappa_e$  by looking for new materials with complex band structures, like heavy fermion compounds.
- Controlling the disorder in materials (such as Skutterudites or Clathrates) to present a rattling effect which causes, ( $\uparrow$ )  $\sigma$  and decreases ( $\downarrow$ )  $\kappa_L$  (see for instance ref. [15]).
- Developing nanostructured materials that could lead to ( $\uparrow$ )  $\alpha$  due to quantum confinement effects, while  $\downarrow \kappa_L$  due to the scattering of phonons at the interfaces. The latest improvements in the  $ZT$  of different materials has been achieved by this approach.

In 1993, Hicks and Dresselhaus pioneered the concept of nanostructuring in design of thermoelectric materials (i.e.  $\text{Bi}_2\text{Te}_3$ ). The addition of the dimensionality

and size of the system is added as a new parameter that affects the coupling of the electrical conductivity, Seebeck coefficient, and thermal conductivity, leading to substantially enhanced ZT [16–18]. Two ideas are dominant for the low-dimensional materials approach for improving ZT. Firstly, the presence of nanoscale constituents would introduce quantum confinement effects to enhance Seebeck coefficient and the power factor  $\alpha^2\sigma$ . Secondly, the numerous internal nano-inclusions and interfaces found in nanostructures would be designed so that the thermal conductivity would be reduced more than the electrical conductivity, based on differences in their respective scattering lengths [16].

As the dimensionality is decreased from 3D crystalline solids to 2D (quantum wells) to 1D (quantum wires) and finally to 0D (quantum dots), the spatial confinement are introduced that create the possibilities to tune the TE properties  $\alpha$ ,  $\sigma$ , and  $\kappa$  independently. When the system size decreases and approaches the scale comparable to the feature length of electron behavior (e.g. mean free path and wavelength) in any direction, the electronic density of states (D.O.S.) can split and become narrow as well as increase substantially (**Figure 4a**), resulting in the enhancement of  $\alpha$ . Meanwhile, the thermal conductivity is also reduced because of the extensive phonon scattering at the surface, interfaces, and grain boundaries, as any dimension is less than the mean free path of phonons. **Figure 4(b)** illustrates

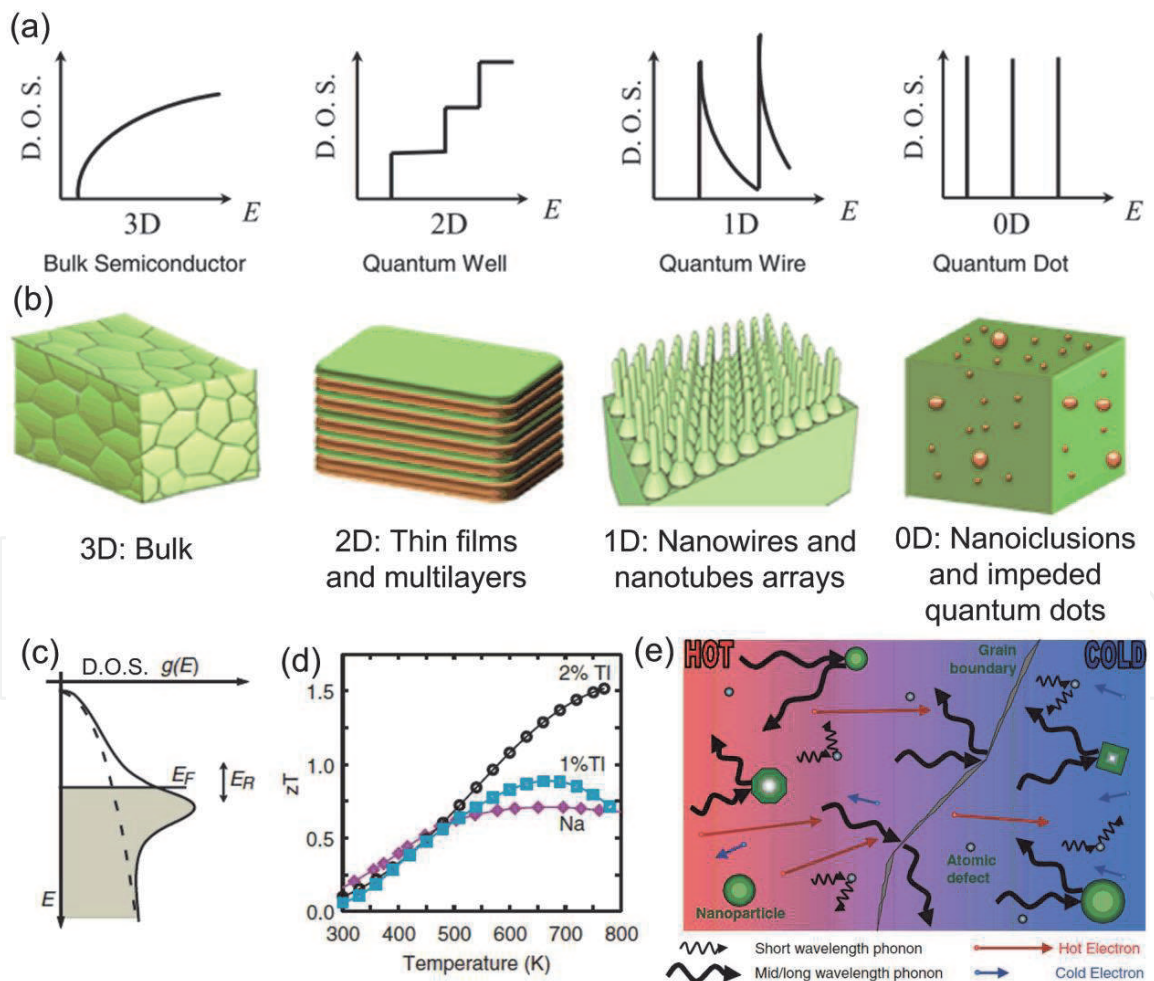


**Figure 4.** (a) Electronic density of states (D.O.S.) for a bulk 3D crystalline semiconductor, a 2D quantum well, a 1D nanowire or nanotube, and a 0D quantum dot [16]. (b) Examples of different nanostructuring with different dimensionalities [14]. (c) A spike in the density of states (dashed line) above the bulk value (solid line) occurs due to resonant states in Tl-doped PbTe [19]. (d) The measured ZT of Tl-PbTe and Na-PbTe samples for 300–800 K indicates an improvement due to the addition of Tl [19]. (e) Schematic diagram illustrating various phonon scattering mechanisms within a thermoelectric material, along with electronic transport of hot and cold electrons [20].

examples of different nanostructuring with different dimensionalities [14]. A schematic diagram is shown in **Figure 4(e)** capturing these various phonon scattering mechanisms, along with the electrical transport within a thermoelectric material. For example, in material embedded nano-inclusions (nanoparticles), atomic defects are effective at scattering short wavelength phonons, but larger embedded nanoparticles are required to scatter mid- and long-wavelength phonons effectively. Grain boundaries can also play an effective role in scattering these longer-wavelength phonons [20].

**Figure 5** plots major milestones achieved for ZT over the past several decades as a function of both year and temperature [20]. In the 1950s,  $\text{Bi}_2\text{Te}_3$  was first investigated as a material of great thermoelectric with  $ZT \sim 0.6$  near room temperature [5, 6]. It was quickly realized that alloying with  $\text{Sb}_2\text{Te}_3$  and  $\text{Bi}_2\text{Se}_3$  allowed for the fine tuning of the carrier concentration alongside a reduction in lattice thermal conductivity. These compounds have played a dominant role in the field of thermoelectrics through today. The alloys of  $\text{Bi}_2\text{Te}_3$  with  $\text{Sb}_2\text{Te}_3$  (such as  $\text{Bi}_{0.5}\text{Sb}_{1.5}\text{Te}_3$ ; p type) and of  $\text{Bi}_2\text{Te}_3$  with  $\text{Bi}_2\text{Se}_3$  (such as  $\text{Bi}_2\text{Te}_{2.7}\text{Se}_{0.3}$ ; n type), with a  $ZT \sim 1$  at room temperature are traditional cooling materials [6]. In recent year, great enhancements in ZT owing to low dimension and nanostructure materials have been reported [19–32] and achieved the highest ZT value of approximately 2.4.

### 1.5 Overview of thermoelectric applications

The solid-state devices based on TE effect have the inherent advantages of reliability, silent and vibration-free operation (no moving fluids or moving parts), a very high power density, and the ability to maintain their efficiency in small scale applications where only a moderate amount of power is needed [19].

Commercial use has been made mostly from Peltier's thermoelectric cooling (TEC) effect in applications, as demonstrated in **Figure 6** [35]:

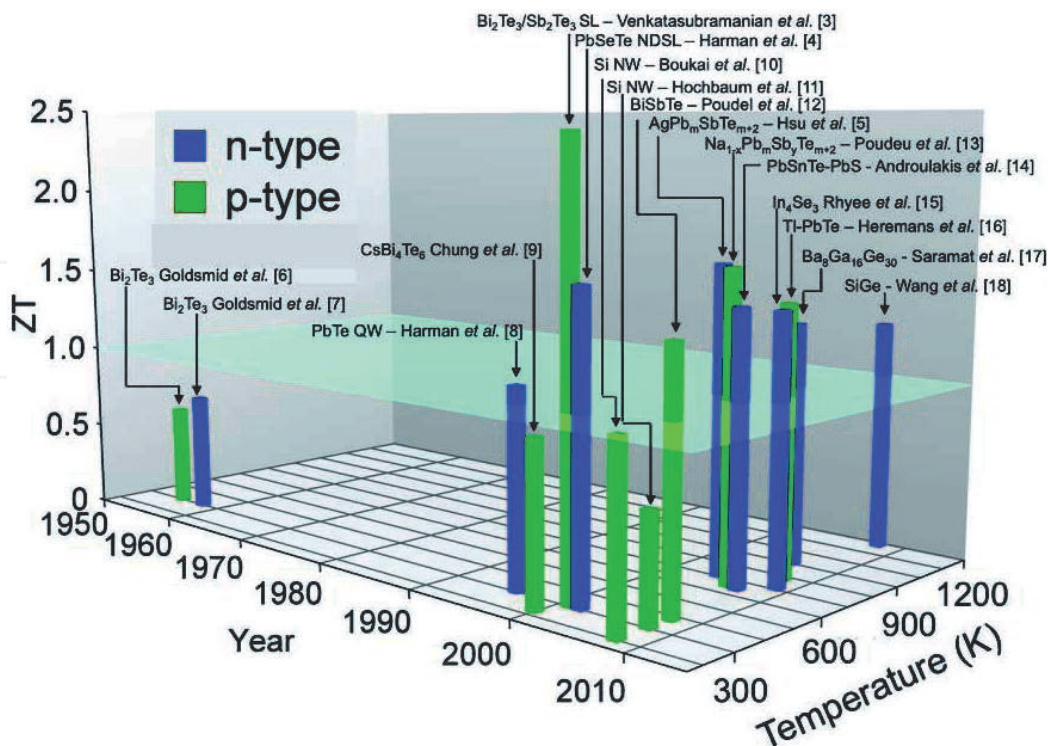


**Figure 5.** Thermoelectric figure-of-merit ZT as a function of temperature and year illustrating important milestones [20]. Although there have been several demonstrations of  $ZT > 1$  in the past decade (2001–2010), no material has yet achieved the target goal of  $ZT \geq 3$ . The material systems that have achieved  $ZT > 1$  have all been based on some form of nanostructuring.

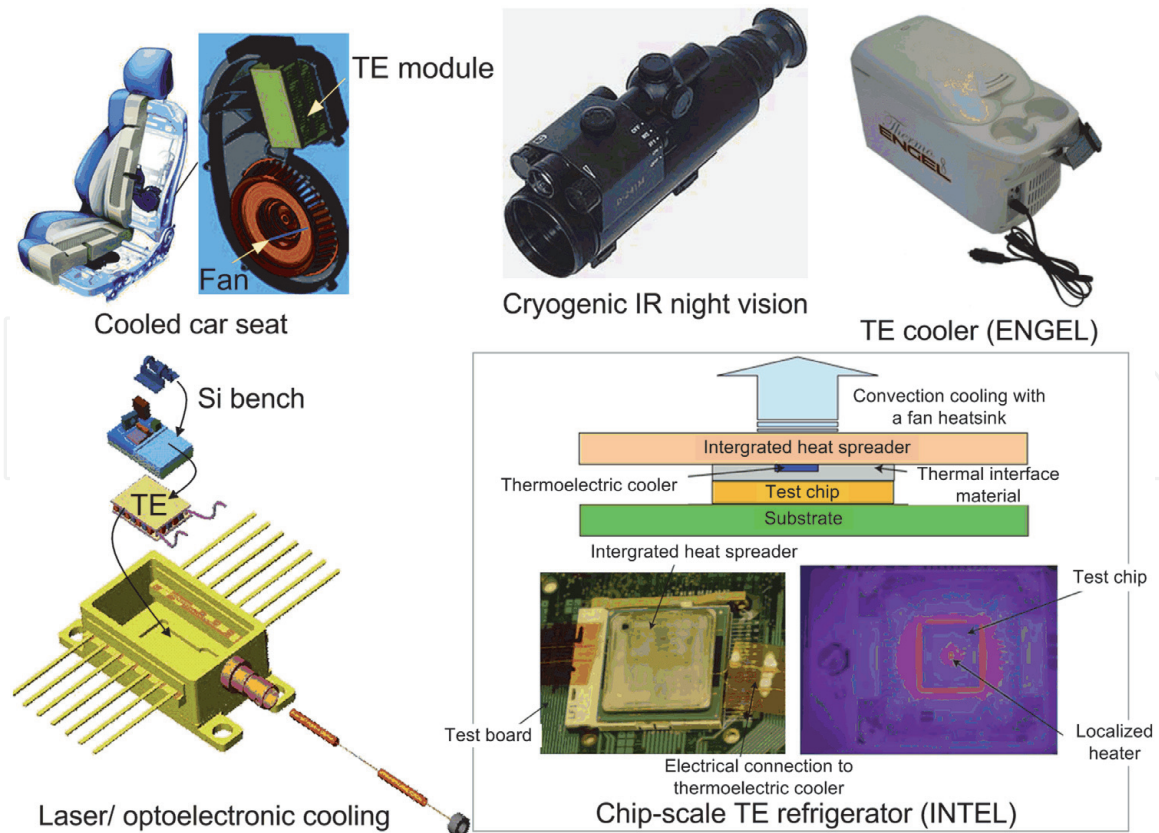


**Figure 6.**  
Overview of potential thermoelectric cooling (TEC) applications [33, 34].

- Small refrigerator devices are used for camping and outdoor activities. For example, the cooler/warmer TE device (Engel Thermo 8) has volume 8 L and weighing just over 3 kg. Its features include cooling performance up to 22°C below ambient temperature and warming up to +65°C.
- Gentherm designed and developed Automotive Climate Control Seat [36], which has TE heat pumps in the back and bottom cushions. The TE system makes conditioned flowing air through channels to the occupant for providing on-demand cooling or heating. As shown in the first panel in **Figure 6**, the seat has the heat pump consisting of a TE module (green box) and a fan (orange).
- Thermal management of tiny laser diodes is used in fiber optic telecom, datacom backhaul networks. TEC can also be used for contact cooling of semiconductor lasers, infrared detectors, CCD- matrix, and miniconditioners for photomultipliers.
- Localized cooling at hot spots of chips was created. For example, the Intel group is the first to demonstrate both concepts of applying the TE material only to a chip's hottest spots (**Figure 6**) [33, 37]. On the substrate, the researchers grew a 100- $\mu\text{m}$ -thick layered structure, called a superlattice, containing bismuth, tellurium, antimony, and selenium. The structure can pump 1300W/cm<sup>2</sup> heat from the back side of the chip to the heat spreader. The superlattice induced an approximately 6°C temperature drop at the hot spot even before the device was powered up, because it conducts heat better than the grease that bonds the rest of the heat spreader to the chip. Yet, when a 3 A-current went through the thermoelectric cooler, the total temperature change was only of 15°C. Managing heat in electronics is a common issue, and TE

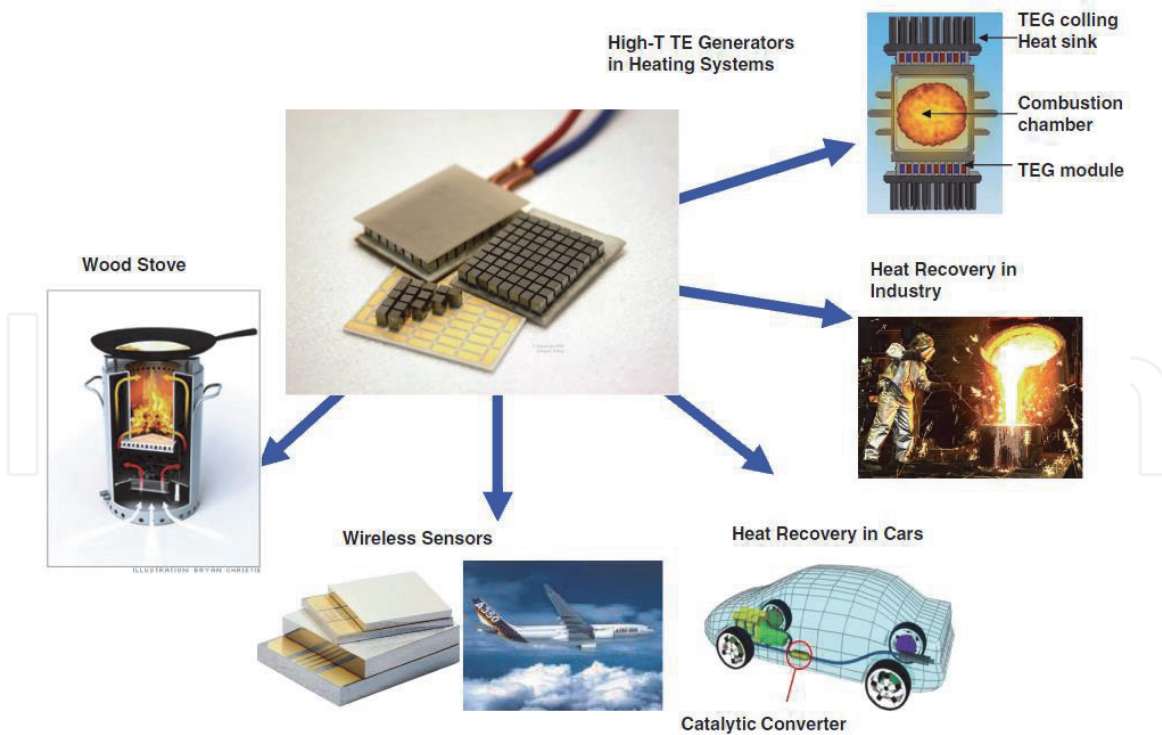


**Figure 7.** Overview of potential thermoelectric generator (TEG) applications [33, 34].

coolers can improve electronic systems in thermal performance, cost, noise, weight, size or efficiency.

**Figure 7** shows an overview of the present and potential applications of thermoelectric generators (TEGs) [34]. They include (1) heating systems and water boilers with TEG units which generate the electricity for the control units and pumping systems, (2) the long term perspective of waste heat recovery for medium-scale industrial facilities, (3) waste heat recovery in automobiles and other combustion-engine-powered vehicles for enhanced efficiency and electric current supply of the electronic system, (4) miniaturized autarkic sensor systems powered by an integrated TEG with a wireless data transmitter, (5) ventilated wood stove powered by a thermoelectric generator with enhanced oxygen supply, improves burning process.

## 2. Nanostructured $\text{Bi}_2\text{Te}_3$ -based thermoelectric thin films grown using pulsed laser deposition

### 2.1 PLD growths of nanostructured $\text{Bi}_2\text{Te}_3$ -based thin films

PLD is one of the most convenient thin film growth techniques that uses a high intensity pulsed laser beam as an external energy source to ablate a target, form a plume, and deposit thin films onto a substrate. In practice, a large number of variables affect the properties of the film, such as substrate temperature ( $T_s$ ), background gas pressure ( $P$ ) and laser fluence. **Figure 8** shows a PLD system for preparing thermoelectric thin films [38, 39]. The substrate was heated and maintained at desired  $T_s$  using a thermocouple and a proportional-integral-derivative temperature controller. The thermocouple was buried inside a substrate holder which was heated by a tungsten lamp or electrical resistance heating. The pressure of ambient gas (He, Ar) could be fine-tuned by the needle valve. Laser source can

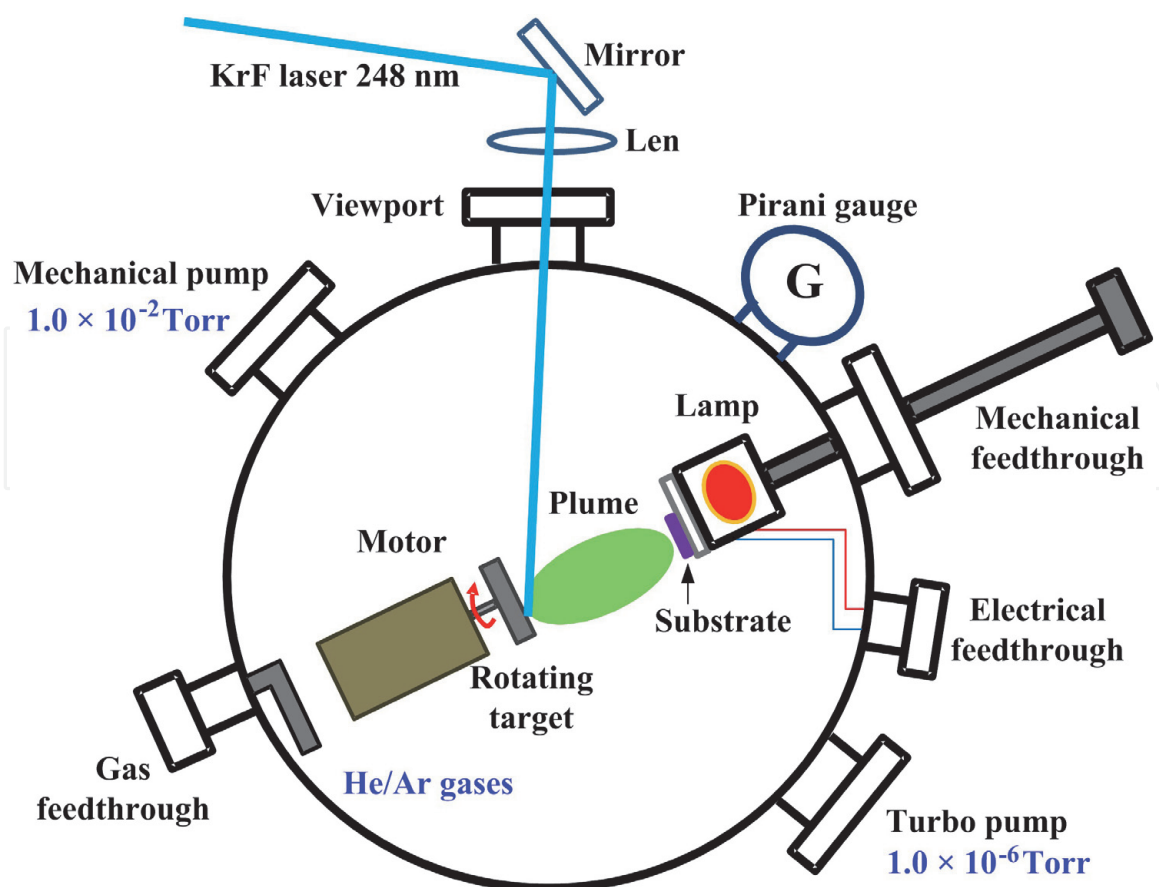


**Figure 8.**  
A schematic illustration of a PLD system.

be KrF excimer laser beam ( $\lambda = 248$  nm) and Q-switched Nd:YAG laser ( $\lambda = 355$  nm) with properly selected laser fluence (e.g., 3.8, 6.2, or 8.3 J/cm<sup>2</sup>) pulsed duration of 5–20 ns, repetition rate of 5–10 Hz [38, 40–42]. The laser beam was guided by several UV mirrors and focused on a stoichiometric polycrystalline target (e.g., Bi<sub>2</sub>Se<sub>3</sub>, Bi<sub>2</sub>Te<sub>3</sub>, Bi<sub>0.5</sub>Sb<sub>1.5</sub>Te<sub>3</sub>, etc.) inside the vacuum chamber by the UV lens. The deposition chamber was evacuated to a base pressure of  $\sim 10^{-6}$  Torr, and high-purity ambient gas (He or Ar) was then introduced until obtaining a target pressure (e.g., usually  $10^{-5} - 3 \times 10^{-1}$  Torr).

The enhancement of the PF of Bi<sub>2</sub>Te<sub>3</sub>-based thin films is challenging due to the coupling among TE material properties [3], and the difficulty in growing stoichiometric films [38]. Indeed, stoichiometry is a key factor for obtaining better TE properties [5, 38, 43–45]. Yet, both tendency for re-evaporation of volatile elements (i.e., Te, Se) at elevated  $T_s$  [45–48] and the low sticking coefficient Te ( $< 0.6$  for Bi<sub>2</sub>Te<sub>3</sub>) at  $T_s$  beyond 300°C [49, 50] constrain to grow stoichiometric Bi<sub>2</sub>Te<sub>3</sub>-based films (Figure 9a and b).

## 2.2 Super-assembling of Bi<sub>2</sub>Te<sub>3</sub> hierarchical nanostructured thin films

C.-H. Chen et al. [41] reported the PLD growths of super-assembling of Bi<sub>2</sub>Te<sub>3</sub> hierarchical nanostructured thin films on the SiO<sub>2</sub>/Si substrates and their thermoelectric properties. Interesting Bi<sub>2</sub>Te<sub>3</sub> super-assemblies were successfully grown using PLD with controlling the substrate temperatures from 350–600°C and at a fixed Ar ambient pressure of approximately  $10^{-3}$  Torr. SEM images in Figure 10 clearly shows the morphological characteristics of the superassembling Bi<sub>2</sub>Te<sub>3</sub> nanostructured thin films [41]. At lower deposition temperatures ( $< 450^\circ\text{C}$ ), the films are mainly composed of vertically aligned nanoscaled flakes, but flakes are

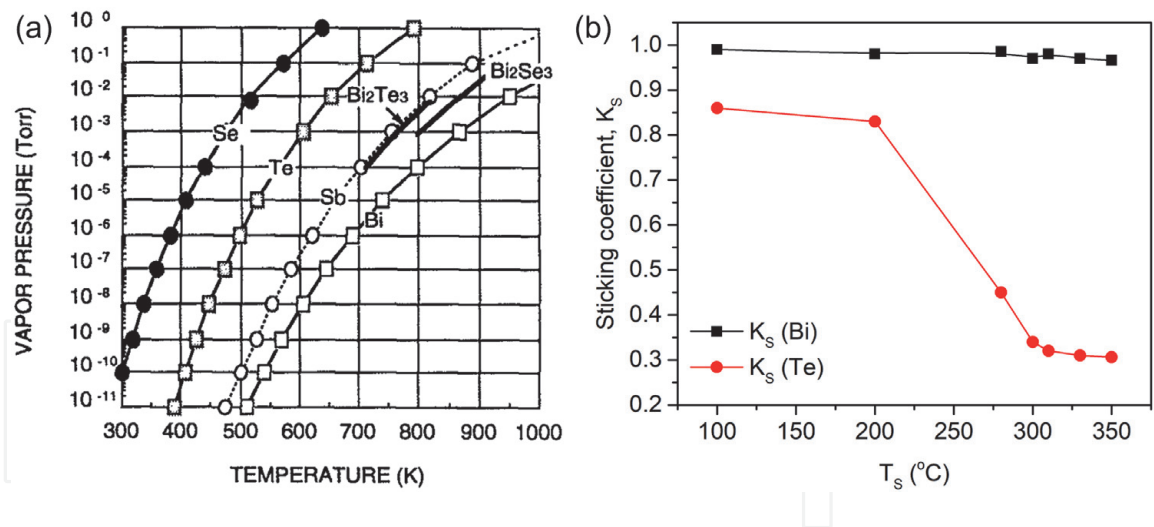


**Figure 9.** (a) Vapor pressures of Bi, Sb, Te, Se,  $\text{Bi}_2\text{Se}_3$ , and  $\text{Bi}_2\text{Te}_3$  as a function of temperature [46]. (b) The variation of sticking coefficient  $K_s$  (Bi, Te) as a function of substrate temperature  $T_s$  at fixed flux ratio  $F_R = 4.5$  [49].

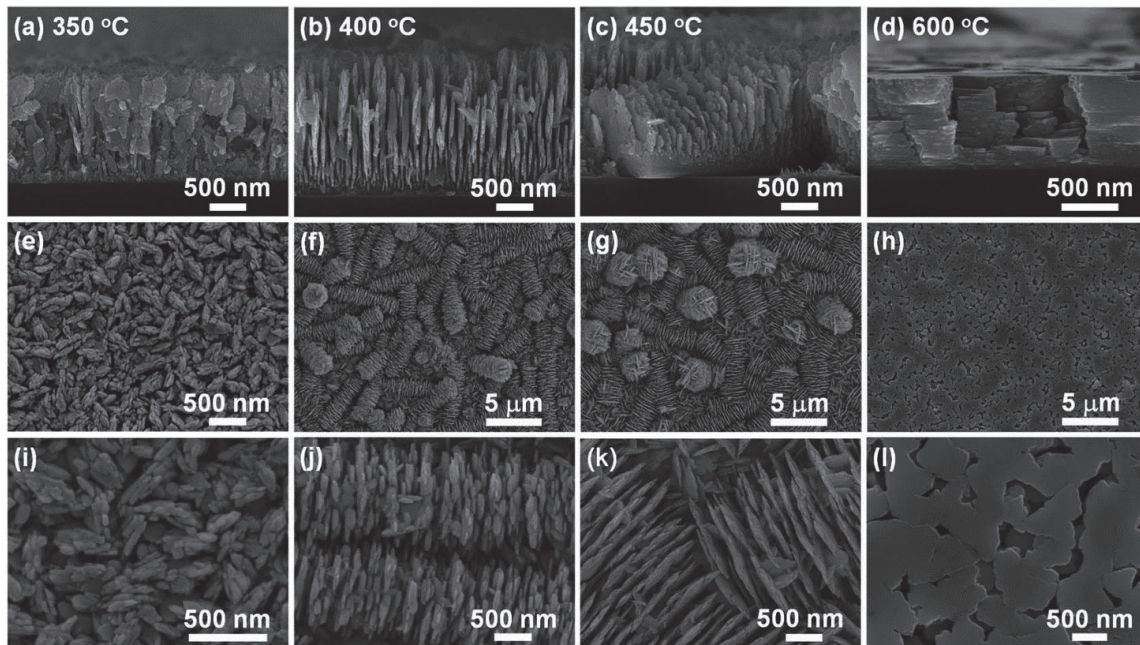


**Figure 10.** (a)–(d) The cross-sectional and (e)–(l) the corresponding top-view SEM images of the  $\text{Bi}_2\text{Te}_3$  superassemblies deposited at 350°C, 400°C, 450°C, and 600°C, respectively [41].

horizontally stacked for 600°C-film (**Figure 10a–d**). Moreover, the bottom of each of the deposited super-assemblies has a relatively continuous and dense layer, and this layer thickness increases with increasing substrate temperature from 350–450°C (**Figure 10a–d**). The top-view SEM images confirm for the high uniformity and presents the unique super-assembling features of the repetitively and regularly assembled nano-flakes (**Figure 10e–h**). These four films are uniformly composed of spindle-like (**Figure 10e**), worm-like (**Figure 10f and g**) and island-like (**Figure 10h**) hierarchical nanostructures. Magnified top-view SEM images (**Figure 10i–k**) further show that the nanoflakes are composed of oriented and regular assemblies of numerous rice-like and elongated primitive nanoparticles [41]. At a higher substrate temperature, thin- and large-size nanoflakes are formed from packing of dense rice-like nanoparticles, driving by the relatively sufficient thermal energy for diffusion. In addition, the out-of-plane superassembly structure (600°C) has a limited column width, which is not always consistent along the out-of-plane direction (**Figure 10d**). Also, the parallel nano-flakes (at 600°C) are

evidently formed by flake stacking along  $c$ -axis orientation or epitaxial-like growth. The special three-dimensional mesh-like structure of 600°C-film would also be an effective design for scattering phonons, and its extremely smooth top surface is certainly beneficial for subsequent analyses and applications [41].

**Figure 11(a)** shows the crystal structure of  $\text{Bi}_2\text{Te}_3$ , which is usually described by a hexagonal cell that consists of 15 layers of atoms stacking along the  $c$ -axis with a sequence [5], namely  $\dots\text{Te}^{(1)}\text{-Bi-Te}^{(2)}\text{-Bi-Te}^{(1)}\dots\text{Te}^{(1)}\text{-Bi-Te}^{(2)}\text{-Bi-Te}^{(1)}\dots\text{Te}^{(1)}\text{-Bi-Te}^{(2)}\text{-Bi-Te}^{(1)}\dots$ . The superscripts refer to two different types of bonding for Te atoms. The 5-atomic-layer thick lamellae of  $\text{-(Te}^{(1)}\text{-Bi-Te}^{(2)}\text{-Bi-Te}^{(1)})\text{-}$  is called quintuple layers, QLs. The  $\text{Te}^{(1)}\dots\text{Te}^{(1)}$  refers Van der Waals force between Te atoms, whereas the  $\text{Te}^{(1)}\text{-Bi}$  and  $\text{Bi-Te}^{(2)}$  are ionic-covalent bonds. This weak binding between the  $\text{Te}^{(1)}\dots\text{Te}^{(1)}$  accounts for the anisotropic thermal and electrical transport properties of  $\text{Bi}_2\text{Te}_3$ . For example, the thermal conductivity along the  $c$ -axis direction ( $\sim 0.7\text{ Wm}^{-1}\text{K}^{-1}$ ) is approximately a half of the value along the plane perpendicular to the  $c$ -axis ( $\sim 1.5\text{ Wm}^{-1}\text{K}^{-1}$ ) [5, 6, 13]. The weak binding of  $\text{Te}^{(1)}\dots\text{Te}^{(1)}$  also make the ease of cleavage along the plane perpendicular to the  $c$ -axis.

**Figure 11(b)** shows XRD patterns of the  $\text{Bi}_2\text{Te}_3$  super-assemblies deposited at various substrate temperatures from 350–600°C. Clearly, all the films exhibited rhombohedral  $\text{Bi}_2\text{Te}_3$  (JCPDS no. 89–4302) without traceable impurities or oxides. When substrate temperature increases, the (00  $l$ ) preferential orientation gradually becomes stronger, the 600°C- film is highly (00  $l$ )-preferred orientation, which is consistent with the SEM observation (**Figure 10d**). The gradually enhanced (00  $l$ ) peaks from 350–450°C mainly originate from the increased thickness of the bottom layer (**Figure 10a–d**), which has similar lamellar morphology with (00  $l$ )-preferential orientation of 600°C-film [41].

**Figure 12** presents the proposed growth model of the super-assembling nano-structured  $\text{Bi}_2\text{Te}_3$  films prepared at various  $T_S$ . The growth mechanisms are layer-then-flake for  $T_S = 350\text{--}450^\circ\text{C}$  and layer-by-layer for higher  $T_S$  of 600°C. We can only find a monotone morphology and single preferential orientation of (00  $l$ ) for 600°C-film, which lead to a fully lamellar morphology with the (00  $l$ ) preferential

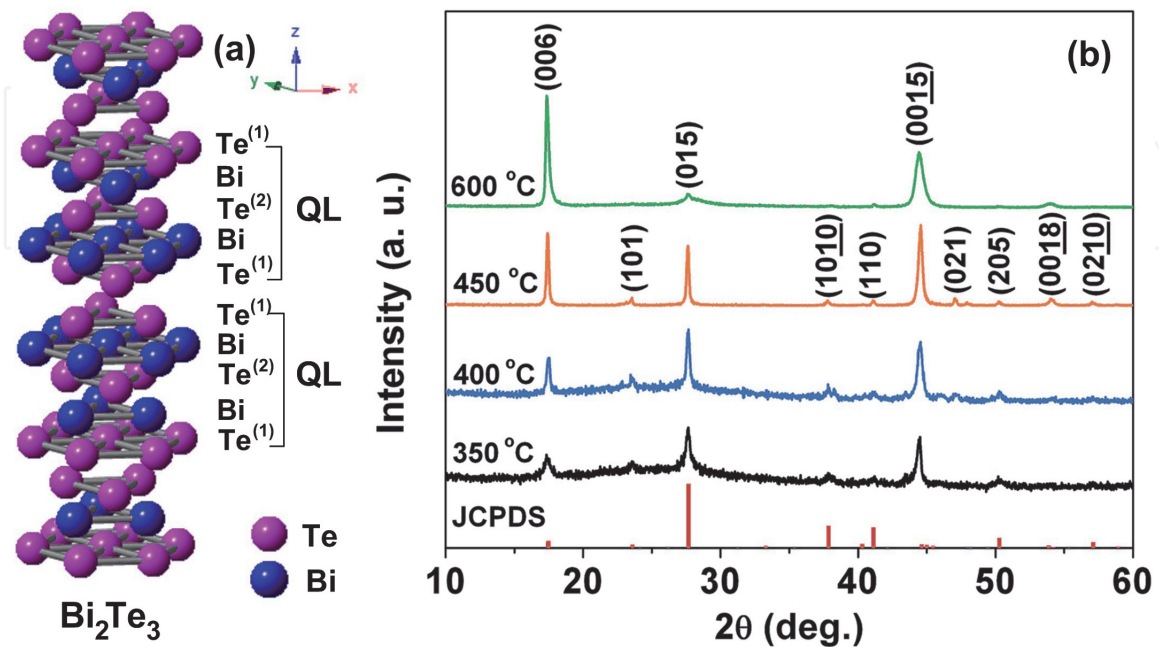


**Figure 11.** (a) Crystal structures of  $\text{Bi}_2\text{Te}_3$ . (b) X-ray diffraction (XRD) patterns of of the  $\text{Bi}_2\text{Te}_3$  super-assemblies deposited at various deposition temperatures from 350–600°C and at an Ar ambient pressure  $\sim 10^{-3}$  Torr [41].

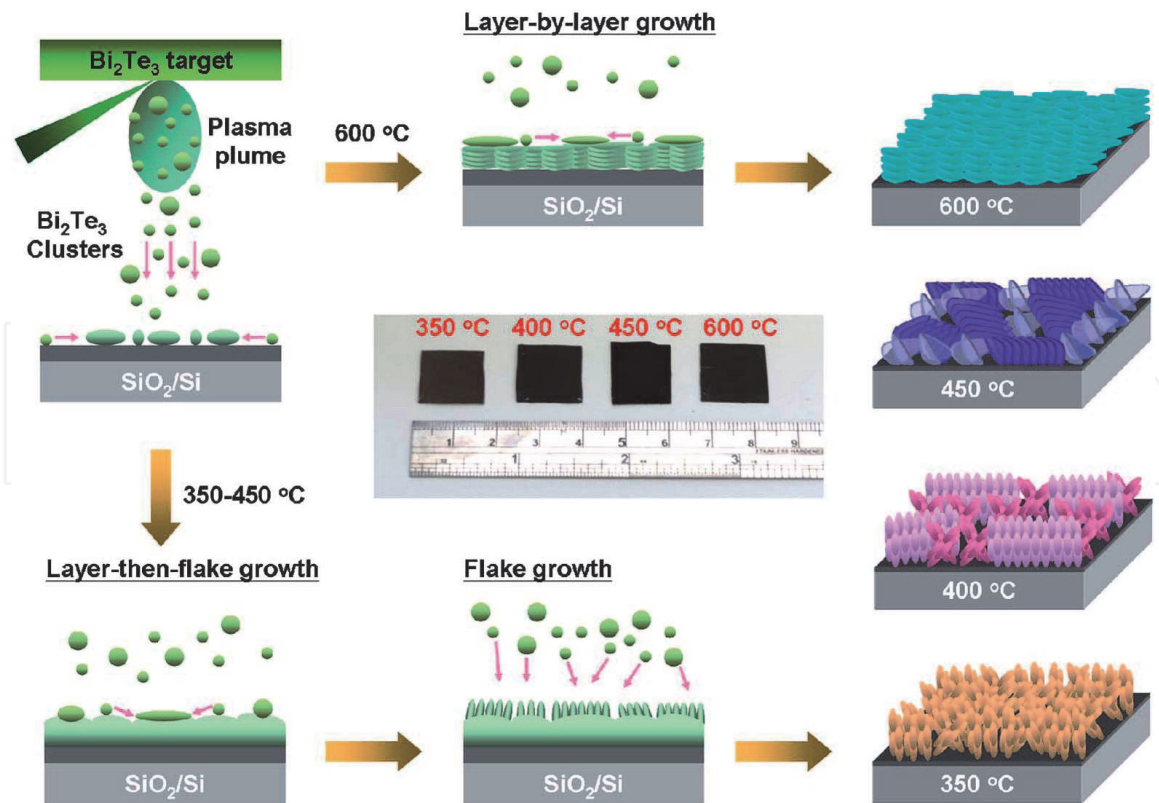


**Figure 12.** Schematic illustration of the layer-then-flake and layer-by-layer growth models and the resulting  $\text{Bi}_2\text{Te}_3$  in-plane ( $350\text{--}450^\circ\text{C}$ ) and out-of-plane ( $600^\circ\text{C}$ ) super-assemblies. Inset is the optical image of the prepared super-assembled films with a size of  $1.5 \times 1.5 \text{ cm}^2$  [41].

orientation. Meanwhile, drastic changes in morphologies from layer to flake and orientations from (00 l) to (015) are observed at lower temperatures ( $350\text{--}450^\circ\text{C}$ ). The (00 l)-preferred orientation should be attributed to the thin bottom layer of the films prepared at  $350\text{--}450^\circ\text{C}$ . The thickness of this layer increases with increasing  $T_s$ . Since the bottom layer at  $350^\circ\text{C}$  is extremely thin, the required  $T_s$  for obtaining layer growth should be just below  $350^\circ\text{C}$ . The drastic change in the morphology and orientation at  $T_s$  of  $350\text{--}450^\circ\text{C}$ , namely, the layer-then-flake growth can be induced by a temperature gradient along the growth direction that the temperature at top surface of the as-deposited film should be slightly lower than at the substrate [41].

**Table 1** summarizes the detailed properties of the super-assembling nanostructured  $\text{Bi}_2\text{Te}_3$  thin-films. Due to such the voided structures, the films exhibited low electrical conductivity from  $49 \text{ S}\cdot\text{cm}^{-1}$  for worm-like superassembly ( $450^\circ\text{C}$ ) to  $160 \text{ S}\cdot\text{cm}^{-1}$  for 3D-layered super-assembly ( $600^\circ\text{C}$ ). Seebeck coefficient of the films was in range of  $113\text{--}138 \mu\text{V}/\text{K}$ . As a result, the power factor (PF) is relatively low in range of  $0.93$  to  $3.0 \mu\text{W}/\text{cmK}^2$ , primarily due to the low electrical conductivity of the films with voided morphologies.

In PLD, tightly controlling substrate temperatures ( $T_s$ ) and ambient pressures ( $P$ ) enables the morphologies and compositions of films to be manipulated extensively, which offers a new method for enhancing the TE properties of films [38, 43, 51, 58, 59]. For example, self-assembled  $\text{Bi}_2\text{Te}_3$  films featuring well-aligned zero- to three-dimensional nanoblocks have been fabricated (**Figure 13a–d**), but the room-temperature PFs of these films remain low ( $\leq 1.9 \mu\text{Wcm}^{-1} \text{ K}^{-2}$ ) [51]. By contrast, A. Li Bassi et al. [43] obtained several microstructured  $\text{Bi}_2\text{Te}_3$  films (**Figure 13e–h**) with high PFs for morphologies: layered-smooth ( $50.6 \mu\text{Wcm}^{-1} \text{ K}^{-2}$ , **Figure 13e, e1**), and compact-smooth ( $21.2 \mu\text{Wcm}^{-1} \text{ K}^{-2}$ , **Figure 13f, f1**) at room-temperature;

| Material                                    | Morphology                  | Method                     | Deposition conditions |         | $n$ ( $10^{19} \text{ cm}^{-3}$ ) | $\mu$ ( $\text{cm}^2/\text{Vs}$ ) | $\sigma$ (S/cm) | $\alpha$ ( $\mu\text{V/K}$ ) | PF ( $\mu\text{W/cmK}^2$ ) | Ref. |
|---|-----------------------------|----------------------------|-----------------------|---------|-----------------------------------|-----------------------------------|-----------------|------------------------------|----------------------------|------|
| $\text{Bi}_2\text{Te}_3$                    | Spindle-like super-assembly | PLD                        | 350°C                 | 0.13 Pa | 4.0                               | 12.4                              | 79              | -113                         | 1.01                       | [41] |
| $\text{Bi}_2\text{Te}_3$                    | Worm-like super-assembly    | PLD                        | 400°C                 | 0.13 Pa | 1.9                               | 25.9                              | 73              | -119                         | 1.03                       | [41] |
| $\text{Bi}_2\text{Te}_3$                    | worm-like super-assembly    | PLD                        | 450°C                 | 0.13 Pa | 1.2                               | 29.4                              | 49              | -138                         | 0.93                       | [41] |
| $\text{Bi}_2\text{Te}_3$                    | 3D-layered super-assembly   | PLD                        | 600°C                 | 0.13 Pa | 5.1                               | 20.3                              | 160             | -137                         | 3.0                        | [41] |
| $\text{Bi}_2\text{Te}_3$                    | Nanoparticles               | PLD                        | 300°C                 | 20 Pa   | 9.7                               | 14.8                              | 230             | -91                          | 1.90                       | [51] |
| $\text{Bi}_2\text{Te}_3$                    | Nanoparticles               | PLD                        | 300°C                 | 1.0 Pa  | 105                               | 8.3                               | 1390            | -60                          | 5.0                        | [52] |
| $\text{Bi}_2\text{Te}_3$                    | Layered Structure           | Sputtering                 | 350°C                 | 1.0 Pa  | 95                                | 12.1                              | 1840            | -70                          | 8.8                        | [52] |
|   | Nanorods                    |                            | 250°C                 | 0.9 Pa  | 9.1                               | 2.0                               | 29              | -81                          | 0.19                       | [51] |
| $\text{Bi}_2\text{Te}_3$                    | Columnar Structure          | Sputtering                 | 350°C                 | 1.0 Pa  | 246                               | 7.5                               | 2990            | -46                          | 6.4                        | [52] |
| $\text{Bi}_2\text{Se}_3$                    | Layered HPs                 | PLD                        | 300°C                 | 40 Pa   | 7.4                               | 81.4                              | 963.8           | -75.8                        | 5.5                        | [38] |
| $\text{Bi}_2\text{Te}_3$                    | Compact film                | PLD                        | 300°C                 | 80 Pa   | 5                                 | 102                               | 814.3           | -172.8                       | 24.3                       | [40] |
| $\text{Bi}_2\text{Te}_3$                    | Layered-smooth film         | PLD                        | 250°C                 | 10 Pa   | 10.1                              | 90.6                              | 1464            | -186                         | 50.6                       | [43] |
| $\text{Bi}_3\text{Se}_2\text{Te}$           | Nanocrystalline film        | PLD                        | 250°C                 | 40 Pa   | 35.5                              | 34.4                              | 1747.5          | -68.8                        | 8.3                        | [53] |
| $\text{Bi}_2\text{Se}_3$                    | Bulk                        | Melting and hot-pressing   |                       |         | —                                 | —                                 | 251.9           | -175                         | 7.7                        | [54] |
| $\text{Bi}_2\text{Se}_{0.3}\text{Te}_{2.7}$ | Bulk                        | Ball milling-hot pressing  |                       |         | —                                 | —                                 | 892             | -190                         | 32.2                       | [55] |
| $\text{Bi}_2\text{Se}_{1.5}\text{Te}_{1.5}$ | Bulk                        | Zone melting               |                       |         | 1.2                               | 230                               | 441.6           | -193                         | 16.5                       | [56] |
| $\text{Bi}_2\text{Se}_{1.8}\text{Te}_{1.2}$ | Nano-platelet bulk          | Polyol method              |                       |         | —                                 | —                                 | 199.6           | -80.9                        | 1.3                        | [57] |
| $\text{Bi}_3\text{Se}_2\text{Te}$           | Bulk                        | Ball milling- hot pressing |                       |         | —                                 | —                                 | 1613            | -60                          | 5.8                        | [55] |

**Table 1.**

Material, type, method, processing conditions, carrier concentration ( $n$ ), mobility ( $\mu$ ), electrical conductivity ( $\sigma$ ), Seebeck coefficient ( $\alpha$ ), power factor ( $\text{PF} = \alpha^2 \sigma$ ) of the  $\text{Bi}_2\text{Te}_3$  films deposited by PLD and RF sputtering, as compared to properties of  $\text{Bi}_2\text{Se}_3$ ,  $\text{Bi}_2\text{Se}_3$ ,  $\text{Bi}_2\text{Se}_x\text{Te}_{1-x}$  bulk and films reported in the literature. All the selected values were recorded at room temperature.

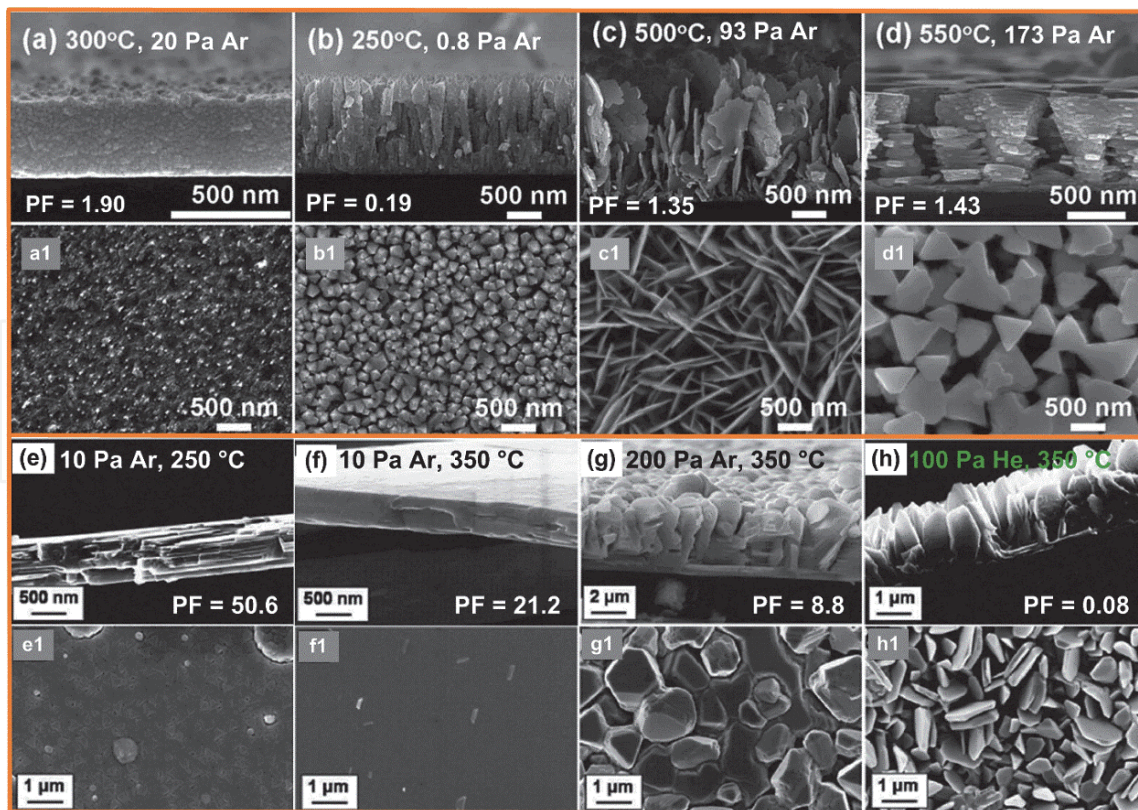


**Figure 13.** The morphology and power factor (unit  $\mu\text{Wcm}^{-1} \text{K}^{-2}$ ) of nano/micro-structured  $\text{Bi}_2\text{Te}_3$  thin-films grown by PLD at various substrate temperatures and ambient pressures, reported by (i) Chang and Chen [51] and (ii) Li Bassi et al. [43].

whereas the PFs remained low values of  $8.8 \mu\text{Wcm}^{-1} \text{K}^{-2}$  for 3D crystallite shapes (Figure 13g,g1) and  $0.08 \mu\text{Wcm}^{-1} \text{K}^{-2}$  for 3D-voided platelets (Figure 13h,h1).

Table 1 summarizes the morphology and properties of  $\text{Bi}_2\text{Te}_3$ -based thin-films deposited by PLD, sputtering, in comparison with the properties of TE bulks. Usually, TE nanomaterials possess low  $\sigma$  values due to the separating or voided structure-morphology, but bulk and thin films have superior  $\sigma$ . For example, the compact-polycrystalline  $\text{Bi}_3\text{Se}_2\text{Te}$  achieved  $\sigma = 1747.5 \text{ S/cm}$  [53] or even higher for some other films [52]. Unfortunately, the  $\kappa$  of films are missed in many published works to calculate ZT of the films. Thermal conductivity ( $\kappa$ ) of nanocrystalline and nanostructured thermoelectrics is expected to achieve low values thanks to the extensive phonons scattering at interfaces, surfaces and grain boundaries. Indeed, reduced  $\kappa$  values have been noted for the monocrystalline  $\text{Bi}_2\text{Se}_{0.3}\text{Te}_{2.7}$  films ( $\kappa = 0.8 \text{ W/m K}$  for an average grain size of 60 nm) [60], and for Bi-Sb-Te films [61, 62].

### 2.3 Thermal conductivity $\kappa$ of $\text{Bi}_2\text{Se}_3$ and $\text{Bi}_2\text{Te}_3$ and Bi-Te-Se compounds

A transient  $3\omega$  technique is usually employed in measuring thermal conductivity of thermoelectric films. The detail of this technique can be found in refs. [62–64]. Table 2 summarizes thermal transport properties (at room-temperature) of nanocrystalline-nanostructured  $\text{Bi}_2\text{Te}_3$ -based thin films and bulk materials in the literature. Generally, the thermal conductivity  $\kappa$  value for polycrystalline films is expected to be smaller than that of bulk alloys because of the extensive phonons scattering at interfaces, surfaces and grain boundaries [5, 60, 66]. Moreover, the  $\kappa$  of nanocrystalline  $\text{Bi}_2\text{Te}_3$ -based films will further decrease when the grain size of

| Sample, fabrication method  | Avg. grain size | $\kappa$ (W/m K)  | $\sigma$ (S/cm) | $\alpha$ ( $\mu$ V/K) | PF = $\sigma\alpha^2$ ( $\mu$ W/cmK <sup>2</sup> ) | ZT (300 K) | Ref. |
|---|-----------------|-------------------|-----------------|-----------------------|--|------------|------|
| Bi <sub>2</sub> Te <sub>2.7</sub> Se <sub>0.3</sub> nanocrystalline thin film, flash evaporation                              | 60 nm           | 0.8 (cross-plane) | 540             | -186.1 (in-plane)     | 18.7 (in-plane)                                    | 0.7        | [60] |
| Sintered bulk Bi <sub>2</sub> Te <sub>3-x</sub> Se <sub>x</sub> material, hot-pressing  | 30 $\mu$ m      | 1.6               | 930             | -177.5                | 29.3   | 0.6        |      |
| Nanocrystalline bismuth-telluride-based (Bi <sub>2</sub> Te <sub>3-x</sub> Se <sub>x</sub> ) thin film                        | 10 nm           | 0.61              | 550             | -84.0                 | 3.9  | 0.19       | [65] |
|   | 27 nm           | 0.68              | 540             | -138.1                | 10.3   | 0.46       |      |
|   | 60 nm           | 0.80              | 540             | -186.1                | 18.7   | 0.70       |      |
| Nanocrystalline Bi-Sb-Te thin film, sputtering  | 26 nm           | 0.46              | 3.3             | —                     | —  | —          | [62] |
|   | 45 nm           | 0.65              | 6.7             | —                     | —  | —          |      |
|   | 84 nm           | 0.81              | 33.3            | —                     | —  | —          |      |
| Nanocrystalline BiSbTe (8:30:62) thin film, flash evaporation   | 150 nm          | 0.6               | —               | —                     | —  | —          | [66] |
| Single crystal BiSbTe bulk alloys   | —               | 0.75              | —               | —                     | —  | —          | [5]  |
| Bi <sub>2</sub> Te <sub>3</sub> /Sb <sub>2</sub> Te <sub>3</sub> superlattices (period~5 nm)                                  | —               | 0.4               | —               | —                     | —  | —          | [67] |
| Bi <sub>2</sub> Te <sub>3+0.63</sub> bulk   | —               | 2.2               | 1000            | -240                  | 58   | 0.87       | [5]  |
| Bi <sub>2</sub> (Te <sub>0.95</sub> Se <sub>0.05</sub> ) <sub>3</sub> bulk  | —               | 1.59              | 901             | -223                  | 45   | 0.85       | [5]  |
| Bi <sub>2</sub> Te <sub>3</sub> /Bi <sub>2</sub> (Te <sub>0.88</sub> Se <sub>0.12</sub> ) <sub>3</sub> superlattice film, MBE | 80 nm           | 1.25              | 639             | -204                  | 27   | 0.60       | [68] |
| Bi <sub>2</sub> Te <sub>3</sub> film, PLD   | —               | 1.1               | —               | —                     | —  | —          | [69] |
| Bi <sub>2</sub> Te <sub>3</sub> /Sb <sub>2</sub> Te <sub>3</sub> superlattices film (layered thickness ~ 6 nm), PLD.          | —               | 0.11              | —               | —                     | —  | —          |      |
| Bi <sub>2</sub> Te <sub>3</sub> films, laser ablation   | —               | 0.2–0.3           | —               | —                     | —  | —          | [70] |
| Bi <sub>x</sub> Sb <sub>2-x</sub> Te <sub>3</sub> nanolayer film, PLD   | 190 nm          | 1.16              | 2700            | 95                    | 25   | 0.65       | [71] |
| Bi <sub>x</sub> Sb <sub>2-x</sub> Te <sub>3</sub> nanodisc film, PLD  | 100 nm          | 1.00              | 1100            | 132                   | 20   | 0.60       |      |
| Bi <sub>x</sub> Sb <sub>2-x</sub> Te <sub>3</sub> nanocolumn film, PLD  | 70 nm           | 0.93              | 280             | 207                   | 12   | 0.39       |      |

**Table 2.**

Room-temperature thermal transport properties of nanocrystalline-nanostructured Bi<sub>2</sub>Te<sub>3</sub>-based thin films and bulk materials in the literature, included: sample and fabrication method, average grain size, thermal conductivity  $\kappa$ , electrical conductivity  $\sigma$ , Seebeck coefficient  $\alpha$ , power factor PF (=  $\alpha^2\sigma$ ), and ZT (at 300 K).

decreases ( $\kappa \leq 0.81$  W/mK, **Figure 14A**) [62, 65]. For Bi<sub>2</sub>Te<sub>3</sub>/Sb<sub>2</sub>Te<sub>3</sub> superlattice films, the coherent backscattering of phonon waves at the superlattice interfaces is outlined for the reduction of lattice thermal conductivity, resulting in the low  $\kappa \leq 0.4$  W/mK [67, 69].

For PLD Bi<sub>2</sub>Te<sub>3</sub>-based films, Yamasaki et al. [69] measured thermal conductivity with an ac calorimetric method in the direction across the film, obtaining  $\kappa \sim 1.1$  W/m K for a Bi<sub>2</sub>Te<sub>3</sub> film deposited by PLD in vacuum (**Table 2**). In addition, Walachova et al. [70] used direct ZT measurement with the Harman method to estimate the  $\kappa$  value, and it is about 0.2–0.3 W/mK for the Bi<sub>2</sub>Te<sub>3</sub> films. Recently, Chang et al. [71] reported the  $\kappa$  values of 0.93–1.16 W/mK for Bi<sub>x</sub>Sb<sub>2-x</sub>Te<sub>3</sub> films with the granular-layered morphologies (**Figure 14B**).

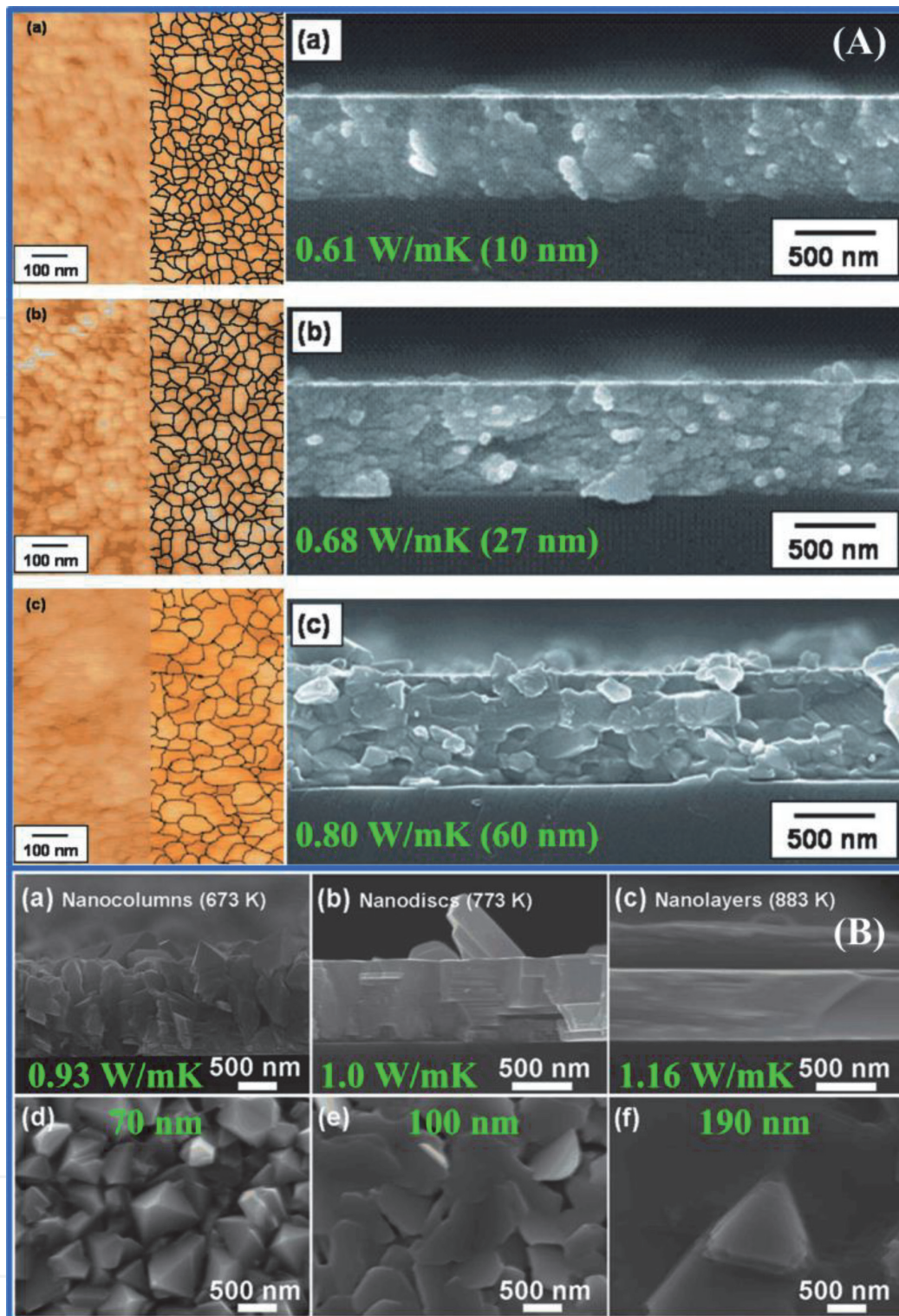


**Figure 14.** The morphology and thermal conductivity of  $\text{Bi}_2\text{Te}_3$ -based films with different grain sizes: (A) nanocrystalline  $\text{Bi}_2\text{Te}_{3-x}\text{Se}_x$  films [65], (B) the  $\text{Bi}_x\text{Sb}_{2-x}\text{Te}_3$  films [71].

### 3. Conclusions

In this book chapter, we present an overview of thermoelectric materials and applications, challenging of enhancing TE properties, and the nanostructuring approach in development TE materials. Various interesting nanostructured  $\text{Bi}_2\text{Te}_3$ -based thin films have been grown successfully by PLD with properly controlled substrate temperatures ambient gas pressures. For example, super-assembling of

$\text{Bi}_2\text{Te}_3$  hierarchical nanostructures were grown at  $T_S$  from 350 to 600°C, and the films possessed relative high Seebeck coefficient of 113–138  $\mu\text{V}/\text{K}$ , but exhibited low electrical conductivities of 49–160  $\text{S}\cdot\text{cm}^{-1}$ , and thus they had relatively low PF in range of 0.93 to 3.0  $\mu\text{W}/\text{cmK}^2$ . Our intensive literature review on  $\text{Bi}_2\text{Te}_3$ -based TE materials can make general conclusion that TE nanomaterials possess low  $\sigma$  values when their structure-morphology are separating or voided, meanwhile, bulk and compact-smooth thin films can achieve high  $\sigma$  values. The PF values of  $\text{Bi}_2\text{Te}_3$ -based thermoelectrics varied in a wide range, i.e. below 5.0  $\mu\text{W}/\text{cmK}^2$  for voided structure-morphology, and reaching intermediate-high PF values of 5.0–50.6  $\mu\text{W}/\text{cmK}^2$  for compact-smooth or compact-layered structures. An advantage of nanocrystalline and nanostructuring thermoelectrics is the reduced thermal conductivity (possibly below  $1 \text{ W}\cdot\text{m}^{-1} \text{ K}^{-1}$ ). This book chapter provides fundamental understanding the relationship amongst processing condition in PLD growths, structure-morphology, and TE properties of  $\text{Bi}_2\text{Te}_3$ -based thin films.

## Acknowledgements

This research is funded by Vietnam National Foundation for Science and Technology Development (NAFOSTED) under grant number 103.02-2019.374, and the Ministry of Science and Technology, Taiwan under Contract Nos. MOST 109-2221-E-214-016 and MOST 110-2221-E-214-013.

## Author details

Le Thi Cam Tuyen<sup>1</sup>, Phuoc Huu Le<sup>2\*</sup> and Sheng-Rui Jian<sup>3,4\*</sup>

1 Department of Physics, Faculty of Basic Sciences, Nam Can Tho University, Can Tho City, Vietnam

2 Department of Physics and Biophysics, Faculty of Basic Sciences, Can Tho University of Medicine and Pharmacy, Can Tho City, Vietnam

3 Department of Materials Science and Engineering, I-Shou University, Kaohsiung, Taiwan

4 Department of Fragrance and Cosmetic Science, College of Pharmacy, Kaohsiung Medical University, Kaohsiung, Taiwan

\*Address all correspondence to: lhuophuoc@ctump.edu.vn and srjian@gmail.com

## IntechOpen

© 2021 The Author(s). Licensee IntechOpen. This chapter is distributed under the terms of the Creative Commons Attribution License (<http://creativecommons.org/licenses/by/3.0>), which permits unrestricted use, distribution, and reproduction in any medium, provided the original work is properly cited. 

## References

- [1] Bell LE. Cooling, heating, generating power, and recovering waste heat with thermoelectric systems. *Science*. 2008; **321**: 1457–1461. DOI: 10.1126/science.1158899
- [2] Chen G., Shakouri A. Heat Transfer in Nanostructures for Solid-State Energy Conversion. *J. Heat Transfer*. 2002; **124**: 242. DOI: 10.1115/1.1448331.
- [3] Snyder GJ, Toberer ES. Complex thermoelectric materials. *Nat. Mater*. 2008; **7**:105–114. DOI: 10.1038/nmat2090
- [4] Li J-F, Liu W-S, Zhao L-D, Zhou M. High-performance nanostructured thermoelectric materials. *NPG Asia Mater*. 2010; **2**: 152. DOI: 10.1038/asiamat.2010.138
- [5] Rowe DM. Thermoelectrics handbook: macro to nano. D.M. Rowe Ed. Boca Raton: CRC Press; 2006. 1014 p. DOI: 10.1201/9781420038903
- [6] Nolas GS, Sharp J, Goldsmid HJ, Thermoelectrics: Basic Principles and New Materials Developments. New York: Springer; 2001.
- [7] Lan Y, Minnich AJ, Chen G, Ren Z. Enhancement of thermoelectric figure-of-merit by a bulk nanostructuring approach. *Adv. Funct. Mater*. 2010; **20**: 357–376. DOI: 10.1002/adfm.200901512
- [8] <http://www.electronics-cooling.com/2005/11/advances-in-high-performance-cooling-for-electronics/>
- [9] Nolas GS, Morelli DT, Tritt TM. KUTTERUDITES: A Phonon-Glass-Electron Crystal Approach to Advanced Thermoelectric Energy Conversion Applications. *Annu. Rev. Mater. Sci*. 1999; **29**: 89. DOI: 10.1146/annurev.matsci.29.1.89.
- [10] Alam H and Ramakrishna S. A review on the enhancement of figure of merit from bulk to nano-thermoelectric materials. *Nano Energy*. 2013; **2**: 190–212. DOI: 10.1016/j.nanoen.2012.10.005
- [11] Pichanusakorn P, Bandaru P. Nanostructured thermoelectrics. *Mater. Sci. Eng. R*. 2010; **67**:19–63. DOI: 10.1016/j.mser.2009.10.001
- [12] Cutler M, Leavy JF, Fitzpatrick RL. Electronic transport in semimetallic cerium sulfid. *Phys. Rev*. 1964; **133**: A1143.
- [13] Tritt TM. Thermoelectric Phenomena, Materials, and Applications. *Annu. Rev. Mater. Res*. 2011; **41**: 433. DOI: 10.1146/annurev-matsci-062910-100453.
- [14] Martín-González M, Caballero-Calero O, Díaz-Chao P. Nanoengineering thermoelectrics for 21st century: Energy harvesting and other trends in the field. *Renew. Sustain. Energy Rev*. 2013; **24**: 288. DOI: 10.1016/j.rser.2013.03.008.
- [15] Eilertsen J, Li J, Rouvimov S, Subramanian MA. Thermoelectric properties of indium-filled  $\text{In}_x\text{Rh}_4\text{Sb}_{12}$  skutterudites. *J. Alloys Compd*. 2011; **509**: 6289. DOI: 10.1016/j.jallcom.2011.03.057.
- [16] Dresselhaus MS, Chen G, Tang MY, Yang RG, Lee H, Wang DZ, Ren ZF, Fleurial J-P, Gogna P. New Directions for Low-Dimensional Thermoelectric Materials. *Adv. Mater*. 2007; **19**: 1043. DOI: 10.1002/adma.200600527.
- [17] Hicks LD, Dresselhaus MS. Effect of quantum-well structures on the thermoelectric figure of merit. *Phys. Rev. B* 1993; **47**: 12727. DOI: 10.1103/PhysRevB.47.12727
- [18] Hicks LD, Dresselhaus MS. Thermoelectric figure of merit of a one-dimensional conductor. *Phys. Rev. B*

1993; **47**: 16631. DOI: 10.1103/PhysRevB.47.16631

[19] Heremans JP, Jovovic V, Toberer ES, Saramat A, Kurosaki K, Charoenphakdee A, Yamanaka S, Snyder GJ. Enhancement of thermoelectric efficiency in PbTe by distortion of the electronic density of states. *Science*. 2008; **321**: 554–557. DOI: 10.1126/science.1159725

[20] Vineis CJ, Shakouri A, Majumdar A, Kanatzidis MG. Nanostructured thermoelectrics: big efficiency gains from small features. *Adv. Mater.* 2010; **22**: 3970. DOI: 10.1002/adma.201000839.

[21] Androulakis J, Lin C-H, Kong H-J, Uher C, Wu C-I, Hogan T, Cook BA, Caillat T, Paraskevopoulos KM, Kanatzidis MG. Spinodal decomposition and nucleation and growth as a means to bulk nanostructured thermoelectrics: enhanced performance in  $\text{Pb}_{1-x}\text{Sn}_x\text{Te-PbS}$ . *J. Am. Chem. Soc.* 2007; **129**: 9780. DOI: 10.1021/ja071875h.

[22] Rhyee J-S, Lee KH, Lee SM, Cho E, Kim SI, Lee E, Kwon YS, Shim JH, Kotliar G. Peierls distortion as a route to high thermoelectric performance in  $\text{In(4)Se(3-}\delta\text{)}$  crystals. *Nature* 2009; **459**: 965. DOI: 10.1038/nature08088.

[23] Saramat A, Svensson G, Palmqvist AEC, Stiewe C, Mueller E, Platzek D, Williams SGK, Rowe DM, Bryan JD, Stucky GD. Large thermoelectric figure of merit at high temperature in Czochralski-grown clathrate  $\text{Ba}_8\text{Ga}_{16}\text{Ge}_{30}$ . *J. Appl. Phys.* 2006; **99**: 023708. DOI: 10.1063/1.2163979.

[24] Wang XW, Lee H, Lan YC, Zhu GH, Joshi G, Wang DZ, Yang J, Muto AJ, Tang MY, Klatsky J, Song S, Dresselhaus MS, Chen G, Ren ZF. Enhanced thermoelectric figure of merit in nanostructured n-type silicon germanium bulk alloy. *Appl. Phys. Lett.*

2008; **93**: 193121. DOI: 10.1063/1.3027060.

[25] Venkatasubramanian R, Siivola E, Colpitts T, O'Quinn B. Thin-Film thermoelectric devices with high room-temperature figures of merit. *Nature*. 2001; **413**: 597–602. DOI: 10.1038/35098012

[26] Hsu KF, Loo S, Guo F, Chen W, Dyck JS, Uher C, Hogan T, Polychroniadis EK, Kanatzidis MG. Cubic  $\text{AgPb}_m\text{SbTe}_{2+m}$ : bulk thermoelectric materials with high figure of merit. *Science*. 2004; **303**: 818. DOI: 10.1126/science.1092963.

[27] Chung DY, Hogan T, Brazis P, Rocci-Lane M, Kannewurf C, Bastea M, Uher C, Kanatzidis MG.  $\text{CsBi}_4\text{Te}_6$ : A High-Performance Thermoelectric Material for Low-Temperature Applications. *Science* 2000; **287**: 1024. DOI: 10.1126/science.287.5455.1024.

[28] Harman TC, Taylor PJ, Walsh MP, LaForge BE. Quantum dot superlattice thermoelectric materials and devices. *Science*. 2002; **297**: 2229. DOI: 10.1126/science.1072886.

[29] Boukai AI, Bunimovich Y, Tahir-Kheli J, Yu J-K, Goddard WA, Heath JR. Silicon nanowires as efficient thermoelectric materials. *Nature*. 2008; **451**: 168. DOI: 10.1038/nature06458.

[30] Hochbaum AI, Chen R, Delgado RD, Liang W, Garnett EC, Najarian M, Majumdar A, Yang P. Enhanced thermoelectric performance of rough silicon nanowires. *Nature* 2008; **451**: 163. DOI: 10.1038/nature06381.

[31] Poudel B, Hao Q, Ma Y, Lan Y, Minnich A, Yu B, Yan X, Wang D, Muto A, Vashaee D, Chen X, Liu J, Dresselhaus MS, Chen G, Ren Z. High-thermoelectric performance of nanostructured bismuth antimony telluride bulk alloys. *Science*. 2008; **320**: 634. DOI: 10.1126/science.1156446.

- [32] Poudeu PFP, Angelo JD', Downey AD, Short JL, Hogan TP, Kanatzidis MG. High thermoelectric figure of merit and nanostructuring in bulk p-type  $\text{Na}_{1-x}\text{Pb}_m\text{Sb}_y\text{Te}_{m+2}$ . *Angew. Chem. Int. Ed. Engl.* 2006; **45**: 3835. DOI: 10.1002/anie.200600865.
- [33] Chowdhury I, Prasher R, Lofgreen K, Chrysler G, Narasimhan S, Mahajan R, Koester D, Alley R, Venkatasubramanian R. On-chip cooling by superlattice-based thin-film thermoelectrics. *Nat. Nanotechnol.* 2009; **4**: 235. DOI: 10.1038/NNANO.2008.417.
- [34] Nielsch K, Bachmann J, Kimling J, Böttner H. Thermoelectric Nanostructures: From Physical Model Systems towards Nanograined Composites. *Adv. Energy Mater.* 2011; **1**: 713–731. DOI: 10.1002/aenm.201100207
- [35] <http://www.electronics-cooling.com/2011/09/thin-film-thermoelectrics-today-and-tomorrow/>
- [36] Heremans JP, Dresselhaus MS, Bell LE, Morelli DT. When thermoelectrics reached the nanoscale. *Nat. Nanotechnol.* 2013; **8**: 471. DOI: 10.1038/nnano.2013.129.
- [37] <http://spectrum.ieee.org/computing/hardware/intelled-team-demonstrates-first-chipscale-thermoelectric-refrigerator>
- [38] Le PH, Liao C-N, Luo CW, Lin J-Y, Leu J. Thermoelectric properties of bismuth-selenide films with controlled morphology and texture grown using pulsed laser deposition. *Appl. Surf. Sci.* 2013; **285P**: 657–663. DOI: 10.1016/j.apsusc.2013.08.107
- [39] Le PH, Luo CW. Thermoelectric and Topological Insulator Bismuth Chalcogenide Thin Films Grown Using Pulsed Laser Deposition. INTECH, UK. 2016; 55–84 DOI: 10.5772/65898
- [40] Le PH, Liao C-N, Luo CW, Leu J. Thermoelectric properties of nanostructured bismuth-telluride thin films grown using pulsed laser deposition. *J. Alloy. Compd.* 2014; **615**: 546–552. DOI: 10.1016/j.jallcom.2014.07.018
- [41] Chang H-C, Chen T-H, Whang W-T, Chen C-H. Superassembling of  $\text{Bi}_2\text{Te}_3$  hierarchical nanostructures for enhanced thermoelectric performance. *J. Mater. Chem. A* 2015; **3**: 10459–10465. DOI: 10.1039/c5ta00911a.
- [42] Chen T-H, Lin P-Y, Chang H-C, Chen C-H. Enhanced thermoelectricity of three-dimensionally mesostructured  $\text{Bi}_x\text{Sb}_{2-x}\text{Te}_3$  nanoassemblies: from micro-scaled open gaps to isolated sealed mesopores, *Nanoscale.* 2017; **9**: 3283. DOI: 10.1039/c7nr00132k.
- [43] Li Bassi A, Bailini A, Casari CS, Donati F, Mantegazza A, Passoni M, Russo V, Bottani CE. Thermoelectric properties of Bi-Te films with controlled structure and morphology. *J. Appl. Phys.* 2009; **105**: 124307. DOI: 10.1063/1.3147870
- [44] Makala RS, Jagannadham K, Sales BC. Pulsed laser deposition of  $\text{Bi}_2\text{Te}_3$ -based thermoelectric thin films. *J. Appl. Phys.* 2003; **94**: 3907. DOI: 10.1063/1.1600524.
- [45] Goncalves LM, Couto C, Alpuim P, Rolo AG, Völklein F, Correia JH. Optimization of thermoelectric properties on  $\text{Bi}_2\text{Te}_3$  thin films deposited by thermal co-evaporation. *Thin Solid Films.* 2010; **518**: 2816. DOI: 10.1016/j.tsf.2009.08.038.
- [46] Noro H, Sato K, Kagechika H. The thermoelectric properties and crystallography of Bi-Sb-Te-Se thin films grown by ion beam sputtering. *J. Appl. Phys.* 1993; **73**: 1252–1260. DOI: 10.1063/1.353266
- [47] Navrátil J, Horák J, Plecháček T, Kamba S, Lošťák P, Dyck JS, Chen W, Uher C. Conduction band splitting and

- transport properties of  $\text{Bi}_2\text{Se}_3$ . *J. Solid State Chem.* 2004; **177**: 1704. DOI: 10.1016/j.jssc.2003.12.031.
- [48] Hor Y, Richardella A, Roushan P, Xia Y, Checkelsky J, Yazdani A, Hasan M, Ong N, Cava R. p-type  $\text{Bi}_2\text{Se}_3$  for topological insulator and low-temperature thermoelectric applications. *Phys. Rev. B.* 2009; **79**: 195208. DOI: 10.1103/PhysRevB.79.195208.
- [49] Mzerd A, Sayah D, Tedenac JC, Boyer A. Crystal growth and sticking coefficient of  $\text{Bi}_2\text{Te}_3$  thin films on Si(1 1 1) substrate. *J. Mater. Sci. Lett.* 1995; **14**: 194. DOI: 10.1007/BF00318254
- [50] Peranio N, Winkler M, Bessas D, Aabdin Z, König J, Böttner H, Hermann RP, Eibl O. Room-temperature MBE deposition, thermoelectric properties, and advanced structural characterization of binary  $\text{Bi}_2\text{Te}_3$  and  $\text{Sb}_2\text{Te}_3$  thin films. *J. Alloys Compd.* 2012; **521**: 163. DOI: 10.1016/j.jallcom.2012.01.108.
- [51] Chang H-C, Chen C-H. Self-assembled bismuth telluride films with well-aligned zero- to three-dimensional nanoblocks for thermoelectric applications. *CrystEngComm.* 2011; **13**: 5956. DOI: 10.1039/c1ce05350g
- [52] Deng Y, Liang H-M, Wang Y, Zhang Z-W, Tan M, Cui J-L. Growth and transport properties of oriented bismuth telluride films. *J. Alloys Compd.* 2011; **509**: 5683–4587. DOI:10.1016/j.jallcom.2011.02.123
- [53] Tuyen LTC, Le PH, Luo CW, Leu J. Thermoelectric properties of nanocrystalline  $\text{Bi}_3\text{Se}_2\text{Te}$  thin films grown using pulsed laser deposition. *J. Alloy. Compd.* 2016; **673**: 107–114. DOI: 10.1016/j.jallcom.2016.03.006
- [54] Sun G, Qin X, Li D, Zhang J, Ren B, Zou T, Xin H, Paschen SB, Yan X. Enhanced thermoelectric performance of n-type  $\text{Bi}_2\text{Se}_3$  doped with Cu. *J. Alloys Compd.* 2015; **639**: 9–14. DOI: 10.1016/j.jallcom.2015.03.124.
- [55] Liu W, Lukas KC, McEnaney K, Lee S, Zhang Q, Opeil CP, Chen G, Ren Z. Studies on the  $\text{Bi}_2\text{Te}_3$ – $\text{Bi}_2\text{Se}_3$ – $\text{Bi}_2\text{S}_3$  system for mid-temperature thermoelectric energy conversion. *Energy Environ. Sci.* 2013; **6**: 552–560. DOI: 10.1039/c2ee23549h
- [56] Wang S, Tan G, Xie W, Zheng G, Li H, Yang J, Tang X. Enhanced thermoelectric properties of  $\text{Bi}_2(\text{Te}_{1-x}\text{Se}_x)_3$ -based compounds as n-type legs for low-temperature power generation. *J. Mater. Chem.* 2012; **22**: 20943. DOI: 10.1039/c2jm34608
- [57] Soni A, Yanyuan Z, Ligen Y, Aik MKK, Dresselhaus MS, Xiong Q. Enhanced thermoelectric properties of solution grown  $\text{Bi}_2\text{Te}_{3-x}\text{Se}_x$  nanoplatelet composites. *Nano Lett.* 2012; **12**: 1203–1209. DOI: 10.1021/nl2034859
- [58] Bailini A, Donati F, Zamboni M, Russo V, Passoni M, Casari CS, Li Bassi A, Bottani CE. Pulsed laser deposition of  $\text{Bi}_2\text{Te}_3$  thermoelectric films. *Appl. Surf. Sci.* 2007; **254**: 1249. DOI: 10.1016/j.apsusc.2007.09.039.
- [59] Obara H, Higomo S, Ohta M, Yamamoto A, Ueno K, Iida T. Thermoelectric Properties of  $\text{Bi}_2\text{Te}_3$ -Based Thin Films with Fine Grains Fabricated by Pulsed Laser Deposition. *Jpn. J. Appl. Phys.* 2009; **48**: 085506. DOI: 10.1143/JJAP.48.085506.
- [60] Takashiri M, Takiishi M, Tanaka S, Miyazaki K, Tsukamoto H. Thermoelectric properties of n-type nanocrystalline bismuth-telluride-based thin films deposited by flash evaporation. *J. Appl. Phys.* 2007; **101**: 074301. DOI: 10.1063/1.2717867.
- [61] Liao C-N, Su X-W, Liou K-M, Chu H-S. Electrical and thermal transport properties of electrically

stressed Bi–Sb–Te nanocrystalline thin film. *Thin Solid Films* 2011; **519**: 4394. DOI: 10.1016/j.tsf.2011.02.066.

[62] Liao C-N., Wang Y-C., Chu H-S. Thermal transport properties of nanocrystalline Bi–Sb–Te thin films prepared by sputter deposition. *J. Appl. Phys.* 2008; **104**: 104312. DOI: 10.1063/1.3026728

[63] Wang G, Endicott L, Uher C. Recent advances in the growth of Bi–Sb–Te–Se thin films. *Sci. Adv. Mater.* 2011; **3**: 539–560. DOI: 10.1166/sam.2011.1182

[64] Cahill DG. Thermal conductivity measurement from 30 to 750 K: the  $3\omega$  method. *Rev. Sci. Instrum.* 1990; **61**: 802. DOI: 10.1063/1.1141498.

[65] Takashiri M, Miyazaki K, Tanaka S, Kurosaki J, Nagai D, Tsukamoto H. Effect of grain size on thermoelectric properties of n-type nanocrystalline bismuth-telluride based thin films. *J. Appl. Phys.* 2008; **104**: 084302. DOI: 10.1063/1.2990774.

[66] Takashiri M, Tanaka S, Miyazaki K, Tsukamoto H. Cross-plane thermal conductivity of highly oriented nanocrystalline bismuth antimony telluride thin films. *J. Alloys Compd.* 2010; **490**: L44–L47. DOI: 10.1016/j.jallcom.2009.10.117

[67] Venkatasubramanian R. Lattice thermal conductivity reduction and phonon localizationlike behavior in superlattice structures. *Phys. Rev. B.* 2000; **61**: 3091–3097. DOI: 10.1103/PhysRevB.61.3091

[68] Peranio N, Eibl O, Nurnus J. Structural and thermoelectric properties of epitaxially grown Bi<sub>2</sub>Te<sub>3</sub> thin films and superlattices. *J. Appl. Phys.* 2006; **100**: 114306. DOI: 10.1063/1.2375016.

[69] N. F. Hinsche, B. Yu. Yavorsky, M. Gradhand, M. Czerner, M. Winkler, J. König, H. Böttner, I. Mertig, and P.

Zahn. Thermoelectric Properties of Bi<sub>2</sub>Te<sub>3</sub>/ Sb<sub>2</sub>Te<sub>3</sub> Superlattices. *Phys. Rev. B.* 2012; **86**: 085323. DOI: 10.1103/PhysRevB.86.085323

[70] Walachová J, Zeipl R, Zelinka J, Malina V, Pavelka M, Jelínek M, Studnička V, Lošťák P. High room-temperature figure of merit of thin layers prepared by laser ablation from Bi<sub>2</sub>Te<sub>3</sub> target. *Appl. Phys. Lett.* 2005; **87**: 081902. DOI: 10.1063/1.2001755.

[71] Chang H-C., Chen C-H., Kuo Y-K. Great enhancements in the thermoelectric power factor of BiSbTe nanostructured films with well-ordered interfaces. *Nanoscale.* 2013; **5**: 7017–7025. DOI: 10.1039/c3nr01499a